Check for updates

JGR Solid Earth

RESEARCH ARTICLE
10.1029/2025JB032004

Special Collection:
Alpine mountain belts in 4-dimensions

The Dynamics and Surface Signal of Slab Break-Off in Continental Settings: Insights From 3D Numerical Modeling

Andrea Piccolo[1,2], Arne Spang[1], Lucas H. J. Eskens[3], Nevena Andrić-Tomašević[3], Paul R. Eizenhöfer[4], Eline Le Breton[5], and Marcel Thielmann[1,6]

[1]Bayerisches Geoinstitut, University of Bayreuth, Bayreuth, Germany, [2]Institute for Geophysics and Tectonics, University of Leeds, Leeds, UK, [3]Karlsruhe Institute of Technology, Institute of Applied Geosciences, Karlsruhe, Germany, [4]School of Geographical and Earth Sciences, University of Glasgow, Glasgow, UK, [5]Univ Rennes, CNRS, Géosciences Rennes—UMR 6118, Rennes, France, [6]Institute of Geoscience, Bonn University, Bonn, Germany

Abstract The fate of an oceanic plate that has been subducted over an extended period of time involves slab break-off, which can occur either simultaneously across the entire slab or locally, creating a tear that propagates sub-horizontally. These processes are thought to explain various geological observations, such as the evolution of foreland basins, in particular, the diachronous migration of the sedimentary facies along the orogen, the transition from under- to overfilled deposition, and the spatiotemporal patterns of uplift and subsidence in active orogens. These interpretations remain debated due to the non-unique nature of geological data. To clarify the role of break-off and tearing on the post-collisional evolution of orogens we conducted 42 3D numerical experiments. We focus on a simplified post-collisional setup to isolate the effects of break-off and its lateral propagation along-strike. We analyzed uplift and subsidence data, examining how their spatiotemporal patterns relate to the rheology of the mantle and oceanic plate. Our results indicate that high pressure dependency of the upper mantle viscosity affects the style of slab break-off and tearing: from a scenario in which these processes yield a clear diachronous uplift to one in which these processes seem to not induce any significant surface signal. We show that the tearing velocity is correlated with the average uplift of the orogen. Models that best fit estimations of tearing velocities do not create significant surface deformation. This opens new perspectives on the relation between break-off and tearing processes.

Plain Language Summary When an oceanic plate sinks into the Earth, it can break off. This can happen gradually, with a tear that spreads sideways through the plate. These processes can explain why depocenter of the sedimentary basins shift over time and other surfaces processes. To better understand the impact of slab break-off and tearing, we ran several 3D computer simulations using a simplified model of what happens after continents collide. We focused on studying how Earth's surface responds to the slab break-off and tearing, and we study how the deep mantle rheology can affect them. We found that the rheology of the upper mantle plays a major role in how slab break-off and tearing affect the surface. In some cases, these processes lead to noticeable and time-dependent uplift; in others, there is little or no surface signal. We also found that the speed at which the tear spreads is linked to the overall amount of uplift. Interestingly, the simulations that best match real-world geological observations are the ones where break-off and tearing do not cause major surface changes.

Key Points:

- Numerical study of the physical controls of slab break-off, tearing, and surface deformation
- Slab break-off and tearing are mainly controlled by mantle viscosity, while thermal structure and strength have a secondary impact
- Surface deformation is a function of tearing velocity

Supporting Information:

Supporting Information may be found in the online version of this article.

Correspondence to:

A. Piccolo,
a.piccolo@leeds.ac.uk

Citation:

Piccolo, A., Spang, A., Eskens, L. H. J., Andrić-Tomašević, N., Eizenhöfer, P. R., Le Breton, E., & Thielmann, M. (2026). The dynamics and surface signal of slab break-off in continental settings: Insights from 3D numerical modeling. *Journal of Geophysical Research: Solid Earth*, *131*, e2025JB032004. https://doi.org/10.1029/2025JB032004

Received 21 MAY 2025
Accepted 20 APR 2026

Author Contributions:

Conceptualization: Andrea Piccolo, Arne Spang, Marcel Thielmann
Data curation: Andrea Piccolo, Lucas H. J. Eskens
Funding acquisition: Marcel Thielmann
Methodology: Andrea Piccolo, Marcel Thielmann
Project administration: Marcel Thielmann
Software: Andrea Piccolo, Arne Spang
Supervision: Nevena Andrić-Tomašević, Marcel Thielmann
Visualization: Andrea Piccolo

© 2026. The Author(s).
This is an open access article under the terms of the Creative Commons Attribution License, which permits use, distribution and reproduction in any medium, provided the original work is properly cited.

1. Introduction

The likely fate of a subducted oceanic plate that drives the convergence between two continents is to break-off and sink into the mantle. Break-off occurs when a horizontal section of the slab at a certain depth becomes thinned enough that it cannot sustain the weight of the portion of the slab below it. Slab break-off can occur at once along the width of the slab or can initiate locally and then propagate sub-horizontally along the entire width of the subducting plate. The propagation of the slab break-off along the strike of the break-off is referred to as lateral tearing (Bercovici et al., 2015; Duretz et al., 2012; Schmalholz, 2011; Thielmann & Schmalholz, 2020; Von Blanckenburg & Davies, 1995). The lateral tearing can be caused by the initial break-off, which alters the stress field, promoting necking in the still-attached portion of the slab (Duretz et al., 2014; van Hunen & Allen, 2011; Wortel & Spakman, 2000; Yoshioka & Wortel, 1995).

This process has often been invoked to explain several geological observations in present-day and fossil subduction/collisional settings: the slab gap observed in many tomographies of active subduction zones (e.g., *west*

Writing – original draft: Andrea Piccolo
Writing – review & editing: Andrea Piccolo, Arne Spang, Lucas H. J. Eskens, Nevena Andrić-Tomašević, Paul R. Eizenhöfer, Eline Le Breton, Marcel Thielmann

Hellenic subduction zone, *Hebrides*, *Hindu-Kush*, *Gibraltar subduction zone*, (Kufner et al., 2021; Sun & Bezada, 2020)); the intermediate depth seismic gap observed world-wide (Isacks & Molnar, 1969; Isacks et al., 1968; Wortel & Spakman, 2000); the spatially heterogeneous surface deformation (e.g., Hellenic subduction zone (Wortel & Spakman, 2000), Hebrides (Chatelain et al., 1992), Alps (Fox et al., 2016; Sternai et al., 2019) and central Appenines (Carminati et al., 1998; Fellin et al., 2022)) and the increased seismic activity within the not yet detached portion of the slab (e.g., Gibraltra (Sun & Bezada, 2020), Vrancea (Mitrofan et al., 2016; Sperner et al., 2001), Hindu-Kush (Kufner et al., 2017)). Moreover, the migration of magmatic activity and exhumation of high pressure rocks have been associated with slab break-off and lateral tearing processes (e.g., Ferrari, 2004; Von Blanckenburg & Davies, 1995).

Slab break-off and tearing can have repercussions on the lithosphere, causing either fault reactivation and surface velocities (Chatelain et al., 1992; Garzanti et al., 2018; Spakman & Wortel, 2004). The fault reactivation, uplift, and subsidence are caused by the removal of the slab-pull. After the removal of the slab-pull the lithosphere rebound causes high stresses that might reactivate fault zones. The surface response to the break-off can affect the evolution of the foreland basin and hinterland erosion. For example, in the European Alps, slab break-off can explain the switch from Flysch to Molasse sedimentation at 30 Ma (Kuhlemann, 2007) or the uplift and erosional pattern during the last 5 Myr (Fox et al., 2016; Sternai et al., 2019). There is an open debate regarding the effects of break-off (Garzanti et al., 2018), because there is still no consensus on what the surface signals of break-off are. Moreover, due to inherent limitations and ambiguities of the geophysical constraints, the same data can be interpreted as other processes. For example, the Vrancea seismic event clusters have been interpreted as a consequence of an ongoing breaking-off event (Mitrofan et al., 2016). However, additional tomographies are also consistent with delamination and drip-off events (Koulakov et al., 2010; Sperner et al., 2001). On this ground, it is important to build a clear understanding of how surface deformation is related to slab break-off and how it can be identified in the geological record.

Several forward modeling studies have been undertaken to understand the geodynamical implications of slab detachment and tearing. These studies encompass analytical, numerical, and analog modeling. The central take-home messages of these works are: (a) the importance of the rheology of the slab, which has first-order controls on the timing of detachment (Bercovici et al., 2015; Gerya et al., 2004; Ribe & Xu, 2020; Schmalholz, 2011; Thielmann & Schmalholz, 2020; Ton & Wortel, 1997) and (b) the slab break-off can be approximated as a pure-shear necking instability (Duretz et al., 2012; Schmalholz, 2011). Nevertheless, most of the numerical studies are 0D to 2D simulations that cannot capture the 3D effects of slab tearing.

The pre-existing 3D forward modeling studies, aimed at understanding the dynamics of lateral tearing, have focused on the rheology of the slab and geometrical characteristics of the setup (Andrews & Billen, 2009; Andrić-Tomašević et al., 2023; Boonma et al., 2023; Duretz et al., 2014; Maiti et al., 2024; Von Tscharner et al., 2014), and highlight the importance of structural inheritance and/or the variation of the strike along the lateral propagation of the tearing (Capitanio & Replumaz, 2013; van Hunen & Allen, 2011).

In other 3D numerical experiments slab break-off and tearing have a strong impact on the plate configuration (Andrić-Tomašević et al., 2023; Capitanio, 2014; Capitanio & Replumaz, 2013; Capitanio et al., 2015; Maiti et al., 2024; Menant et al., 2016; Sternai et al., 2014). For example, the interaction between slab break-off, tearing, and trench retreat can enhance mantle heat flow and associated magmatism, and can drive a reorganization of the plate margin, leading to large-scale extrusion and intraplate deformation (Capitanio, 2014; Capitanio et al., 2015; Menant et al., 2016). However, to study the uplift and subsidence rate, it is necessary to simplify the geological scenario. For this reason, we here designed a simplified scenario where we only consider a stalled slab and ignore any effects of far-field plate velocities.

In this contribution, we designed a simplified scenario to extract the vertical surface velocities caused by slab break-off and lateral tearing, minimizing the effects of large-scale processes. In particular, we focus on the effects of slab-break off and tearing on the uplift signals as a function of the thermal structure of the slab and mantle rheology. We performed 42 3D numerical experiments to understand how the velocity of the tearing is affected by these input parameters and how it is correlated with the mean uplift and subsidence rate.

21699356, 2026, 5, Downloaded from https://agupubs.onlinelibrary.wiley.com/doi/10.1029/2025JB032004 by Karlsruher Institut Fur Technologie, Wiley Online Library on [12/11/2026]. See the Terms and Conditions (https://onlinelibrary.wiley.com/terms-and-conditions) on Wiley Online Library for rules of use; OA articles are governed by the applicable Creative Commons License

21699356, 2026, 5, Downloaded from https://agupubs.onlinelibrary.wiley.com/doi/10.1029/2025JB032004 by Karlsruher Institut Fur Technologie, Wiley Online Library on [12/11/2026]. See the Terms and Conditions (https://onlinelibrary.wiley.com/terms-and-conditions) on Wiley Online Library for rules of use; OA articles are governed by the applicable Creative Commons License

2. Method

2.1. Numerical Methods

We carried out 42 experiments using the numerical code *LaMEM* (Kaus et al., 2016). *LaMEM* is a 3D staggered finite-difference code written in C that solves the coupled mass, momentum, and energy conservation equations. The advection of the material properties through time is performed using markers that carry all the material properties of the rock phases and the historical variables such as stress tensor components, total plastic strain, and temperature. The constitutive model that connects stress and strain is visco-elasto-plastic. For further details of the implementation of the constitutive models, see Texts S1 and S2 in Supporting Information S1.

We employ diffusion and dislocation creep mechanisms for the ductile deformation mechanisms and Drucker-Prager (Drucker & Prager, 1952) for brittle failure:

$$\eta_{\text{dif|dis}} = \frac{1}{2} B_{\text{dif|dis}}^{-\frac{1}{n}} \tau^{1-n} \exp\left(\frac{E_{a,\text{dif|dis}} + PV_{a,\text{dif|dis}}}{RT}\right) \tag{1}$$

$$\tau_y = P \sin(\phi) + C \cos(\phi) \tag{2}$$

"dif" and "dis" subscripts indicate diffusion and dislocation creep, respectively. n is the stress exponent (for diffusion creep rheology $n = 1$), B is the pre-exponential factor ($\text{Pa}^{-n}\text{s}^{-1}$), R is the gas constant ($\frac{\text{J}}{\text{Kmol}}$), E_a is the activation energy ($\frac{\text{J}}{\text{mol}}$), T is the temperature (in K), and P is the pressure (Pa). V_a ($\frac{\text{cm}^3}{\text{mol}}$) is the activation volume. In this work, we focus on the activation volume of dislocation creep of the mantle, as it is a poorly constrained value and controls the effective resistance of the mantle against the detachment. B_{dif} is computed using a grain size of 1,000 μm. τ_y is the yield stress, ϕ is the friction angle, and C is the cohesion of the material. In addition, we mimic the low temperature plasticity by introducing a stress limit (τ_{lim}) for the slab, following the strategy of van Hunen and Allen (2011). To reproduce the plastic limit, the friction angle of the slab is reduced to $\phi = 0.001$, while the cohesion is used to impose the stress limiter ($C = \tau_{\text{lim}}$), see Supporting Information S1 for further clarification. In our simulation, we do not introduce damage rheologies (i.e., grain size reduction and plastic weakening). However, we consider the effects of shear heating. Shear heating depends on the deformation rate and on the stress and this source of energy will locally reduce the viscosity (see Supporting Information S1 for further explanation). The cut-off viscosities are 10^{16} and 10^{26} Pas respectively.

The rock density is computed using a reference value (ρ_r) using the following equation:

$$\rho(T) = \rho_r[1 - \alpha(T - T_r)] \tag{3}$$

Where α is the thermal expansivity, and T is the temperature and T_r is the reference temperature (25 °C).

2.2. Initial Setup

All the models share several common properties: we employ a numerical box whose boundary conditions are free-slip in all the faces, except for the top boundary, which does not have a constrained velocity (open top boundary). The energy conservation boundary conditions are isothermal for the bottom and top boundary (20 °C at the top and 1375°C at the bottom) and no heat-flux on the lateral edges and faces of the numerical box. The extent of the numerical domain are 1,600 km (−800 to 800 km) along the x and y directions and 750 km (−700 to 50 km) along the z direction, and we employ 256 cells per direction. x can be interpreted as the direction East to West, while y direction can be interpreted as North to South direction. The number of markers is ∼450 million (27 in each cell), evenly distributed between each cell of the numerical grid, and we employ sub-grid routines to control the markers' population during the simulation (see Text S1 in Supporting Information S1). To simulate the free surface, we employ an internal free surface (sticky air approximation, see Crameri et al. (2012)). We do not employ erosion and sedimentation routines for the current modeling work, as we are interested in the surface signals without the interference of other surface processes. The only constraint that we introduce is to not let the topography to have a local angle to be higher than 45°: if the topography gradient exceeds this cut-off, it is adjusted by shifting the free-surface toward the optimal angle (and changing the properties of the markers accordingly).

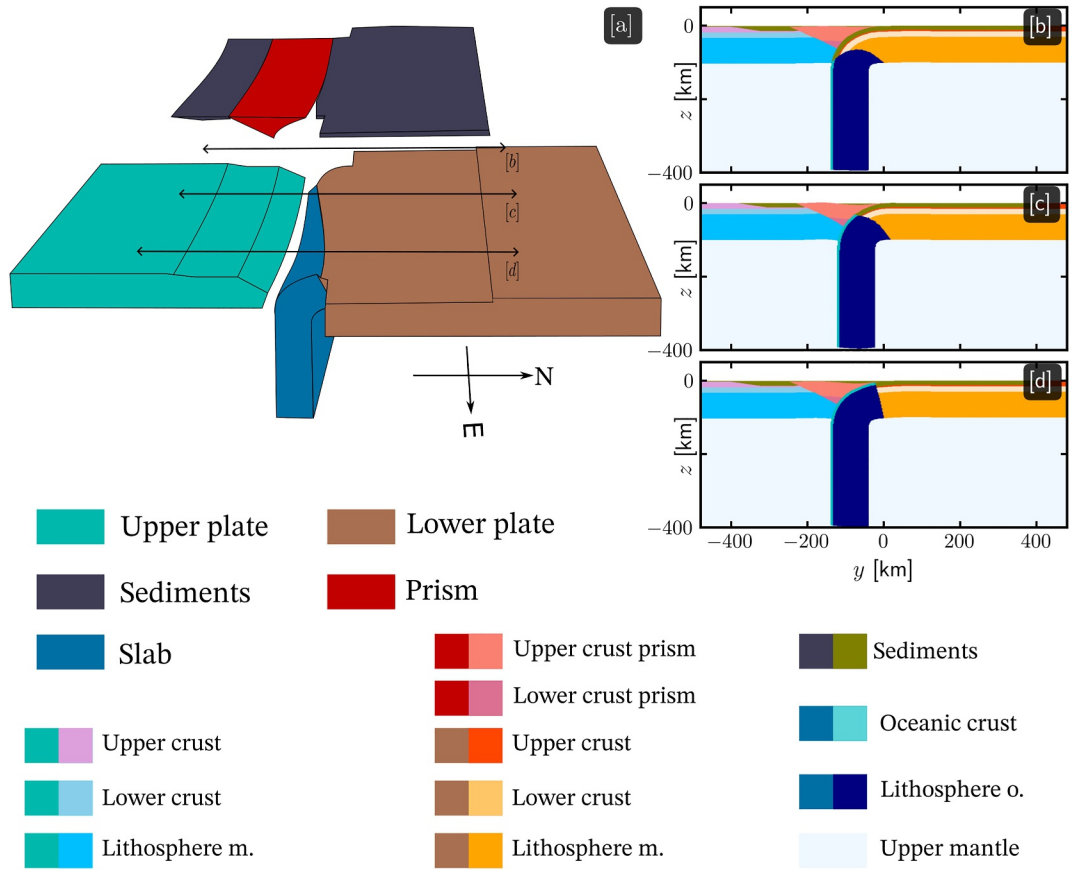


Figure 1. Initial Setup. (a): Initial setup geometry. Each colored volume represents a different macro-unit. (b–d): Three representative sections of the full phase field ($x = -590, 0, 590$ km); these section are highlighted by three black lines in [a]. The temperature field, lithospheric strength, and the initial topography are plotted in Figures S2–S4 of the Supporting Information S1.

For the generation of the initial geometry, we take inspiration from the European Alps (Agard, 2021) (i.e., heterogeneous subduction zone along strike). We introduce several features (i.e., orogenic sedimentary prism, subduction channel), without accounting for their formation and neglecting the subduction and collisional stage. This allows us to controls the initial position of the target area (i.e., *foreland basin*, *or strike of the slab*) of the model. In Figure 1; Figures S2–S4 in Supporting Information S1, we provide three illustrations of the initial setup, the thermal structure of the slab and the major geological units, and rheological structure, and topography. We divide the initial setup into six macro-units (for simplifying the description and visualization): lower continental plate, upper continental plate, sediments unit, and orogenic prism, subducting plate, and background oceanic plate. Each macro-unit may contain multiple different rock phases with different material properties (see Table 1 for further details).

The lower continental plate is placed in the north ($y > 0$ km) and extends from East to West. The southern rim has a 400 km wide sedimentary sequence. The unit has a triangular shape, with the largest depth (~12 km) toward the north, the maximum thickness has been chosen such that the sedimentary sequence is properly resolved. The lower continental plate's thickness is 100 km, the top 30 km are composed of two crustal units (lower and upper crust), and its lowermost unit is a continental lithospheric mantle. The temperature distribution is a double-stage linear geotherm (see Figure S2a in Supporting Information S1).

The upper continental plate covers the southern portion of the numerical model ($y < 0$ km) and has a lateral extent of 1,200 km (−600 to 600 km along x directions). The northern margin has a sedimentary sequence which is identical to the one of the lower continental plate. The other geometrical and thermal properties are the same as in the lower continental plate. The upper continental plate is surrounded by a oceanic plate (which is not shown in

21699356, 2026, 5, Downloaded from https://agupubs.onlinelibrary.wiley.com/doi/10.1029/2025JB032004 by Karlsruher Institut Fur Technologie, Wiley Online Library on [12/11/2026]. See the Terms and Conditions (https://onlinelibrary.wiley.com/terms-and-conditions) on Wiley Online Library for rules of use; OA articles are governed by the applicable Creative Commons License

Table 1
Table of Material Properties

Rock unit	Rheological law	B_{dif} ($Pa^{-1}s^{-1}$)	$E_{a,dif}$ ($kJmoI^{-1}$)	Va, dif (cm^3mol^{-1})	n (n.d.)	B_{dis} ($Pa^{-n}s^{-1}$)	$E_{a,dis}$ ($kJmoI^{-1}$)	$V_{a,dis}$ (cm^3mol^{-1})	ρ_0 (kgm^{-3})	C (MPa)	ϕ (n.d.)
Upper crust (1–2)	Wet Plagioclase(1)	$4.742e-11$	159	38	3.0	$1.130e-15$	345	38	2700	10	30
Lower crust (1–2)	Wet Plagioclase	$4.742e-11$	159	38	3.0	$1.130e-15$	345	38	2750	10	30
Continental mantle lithosphere (1–2)	Dry Olivine(2)	$1.5e-9$	375	5	3.5	$6.22e-16$	530	15	3290	10	30
Oceanic crust	Wet Plagioclase(1)	$4.742e-11$	159	38	3.0	$1.130e-15$	345	38	3300	10	10
Oceanic plate mantle	Dry Olivine	$1.5e-9$	375	5	3.5	$6.22e-16$	530	8	3300	200, 400, 600	0.001
Upper Mantle	Dry Olivine	$1.5e-9$	375	5	3.5	$6.22e-16$	530	8, 10, 11, 12, 13, 15	3300	10	30
Upper orogenic Prism & Sediments	Wet Plagioclase	$4.742e-11$	159	38	3.0	$1.130e-15$	345	38	2700	1	5
Lower orogenic Prism	Dry Plagioclase	2.832	460	24	3.0	$3.205e-17$	641	24	2700	10	30

Note. The activation volume of the dislocation creep of the upper mantle and the oceanic plate are target parameter. All the material have the same G (shear modulus) (GPa), 50 (GPa). α is the same for all the material properties and it is equal to $3e-5$ ($1/K$). C_p is equal is the same for all the phases and is equal to 1050 ($Jkg^{-1}K^{-1}$). k is the same for all the phases and it is equal to 3.0 ($Wm^{-1}K^{-1}$). In this work, A the radiogenic heat production per unit of mass is 0. (1): Rybacki and Dresen (2000), (2): Hirth and Kohlstedt (2003). Lower and upper crust, and continental mantle lithosphere are phases that belongs to both upper and lower plate. The oceanic subducting plate has fixed properties in all experiments, while the activation volume of the mantle is changed within the experiments.

Figure 1), whose temperature is described by a half-space cooling model (see Figure S2b in Supporting Information S1). The idealized collisional zone comprises a triangular-shaped orogenetic prism extending 80 km north, south and downwards.

The subducting plate has a length (L_0) of 400 km, initial bending is computed using the formulation of Ribe (2010) (see Text S4 in Supporting Information S1), initial thickness is 100 km, and a lateral extent is 1,200 km. Without strong thermal-compositional heterogeneities, slab break-off and tearing start at the center of the slab (Andrić-Tomašević et al., 2023; Burkett & Billen, 2010; Duretz et al., 2014; van Hunen & Allen, 2011). To initiate slab tearing from west to east, we introduce a compositional heterogeneity: the total subducted continental lithosphere linearly decreases from 120 to 20 km from west to east along the strike of the subduction zone (in Figure 1 the transition between brown and blue macro units is shifting toward the lower plate from west to east). The temperature field of the slab is computed using a linear combination of a half-space cooling model (with an age of 30 Myr) and the analytical solution of McKenzie (1969)—see Text S4 in Supporting Information S1. The main parameter that defines the thermal structure is the average subduction velocity (v_s) prior to the collision and the stalling of the subducting plate. We test three subduction velocities: 2.5, 5.0 and 10 $\frac{cm}{yr}$ (see Figures S2c–S2e in Supporting Information S1). The lowest subduction velocity represents hot slab scenarios, while the highest represents cold slab scenarios. We tested three different values of the stress limiter $\tau_{lim} = [200, 400, 600]$ MPa, following the parameters used by van Hunen and Allen (2011) and Capitanio and Replumaz (2013). The subducting plate is composed of two rock-phases:oceanic plate crust and oceanic plate lithospheric mantle. The oceanic crust has a low cohesion and friction angle to lubricate the plate interface see Table 1 and wet plagioclase rheological flow law (Rybacki & Dresen, 2000). The oceanic plate lithospheric mantle viscous flow law is dry olivine (Hirth & Kohlstedt, 2003). The parameters of the viscous law of the oceanic lithospheric mantle have been kept constant in all experiments such that the timescales of the necking instabilities are only a function of the thermal state of the slab. We simulate the low temperature plasticity by using a stress limiter (τ_{lim}).

The upper mantle has a constant temperature of 1350°C. The rheological flow law employed for the upper mantle is dry olivine (Hirth & Kohlstedt, 2003). We varied the activation volume of dislocation creep of dry olivine from a minimum of 8 to 15 $\frac{cm^3}{mol}$.

The strength of the orogenic prism is determined by the same rheology as that of the sediments. We additionally introduced a small, stiff layer at the base of the prism to simulate a strong, metamorphosed lower crust. This small

21699356, 2026, 5, Downloaded from https://agupubs.onlinelibrary.wiley.com/doi/10.1029/2025JB032004 by Karlsruher Institut Fur Technologie, Wiley Online Library on [12/11/2026]. See the Terms and Conditions (https://onlinelibrary.wiley.com/terms-and-conditions) on Wiley Online Library for rules of use; OA articles are governed by the applicable Creative Commons License

21699356, 2026, 5, Downloaded from https://agupubs.onlinelibrary.wiley.com/doi/10.1029/2025JB032004 by Karlsruher Institut Fur Technologie, Wiley Online Library on [12/11/2026]. See the Terms and Conditions (https://onlinelibrary.wiley.com/terms-and-conditions) on Wiley Online Library for rules of use; OA articles are governed by the applicable Creative Commons License

portion has been prescribed for stabilizing the orogen, and preventing horizontal components that could be interfering with vertical velocities. The rheological structure of the prism is illustrated in Figure S3 of the Supporting Information S1. We do not explicitly simulate the collisional evolution of the orogen; we therefore prescribe a stiffer rheological structure for the prism. Although the orogenic area is weaker than the foreland basins (see Figure S4 in Supporting Information S1), a more realistic rheology may introduce additional processes that affect the effective surface deformation signal, such as the gravitational collapse observed in large hot orogens (Beaumont et al., 2001; Faccenda et al., 2008; Piccolo et al., 2018). We neglect these additional processes to focus specifically on the tearing signal.

Figure S4 in Supporting Information S1 shows the initial topography, computed using simplified isostatic balance equations (Turcotte & Schubert, 2014). After applying the isostatic balance, and before starting the simulation, we modify the collisional zone trench adding another sediments to avoid high topographic gradients (in Figure 1, this unit is merged with the other sedimentary units). Moreover, we run thermal diffusion for 1 million years before starting the simulation, smoothing the temperature gradients in the numerical domain.

3. Results

We test mainly three parameters: τ_{lim} (the stress limiter), v_s (the average sinking velocity of the slab prior the collision), and $V_{a,\text{dis}}$ of the mantle (activation volume of dislocation creep). v_s controls the thermal structure of the slab and its viscosity and buoyancy, τ_{lim} controls the maximum stress that the slab can bear, meanwhile, the $V_{a,\text{dis}}$ controls the average viscosity of the mantle along the slab and its propensity to deform in dislocation creep. The target parameters are the velocity of tearing v_{tearing}, along the trench (x_{trench}) and the surface velocities $\dot{H}$. We additionally monitor the evolution of the normalized thickness ($D^{\dagger} = D(t)/D_0$) and the normalized maximum stress $\tau_{\text{max}} = \tau_{\text{max}}(t)/\tau_{\text{lim}}$ within the necking zone (which is defined as a function of the maximum and minimum depth of lateral tearing). τ_{max} is the maximum stress bear by the slab along its thickness. We will use uplift and subsidence for highlighting positive and negative velocities, respectively.

We define three concepts to easily follow the description of the results:

- *Necking* is a mechanical instability that begins at the start of the simulation and occurs along the width (along the strike) and thickness (perpendicular to the strike) of the slab, as predicted by Von Tscharner et al. (2014). We focus on the necking process that reduces the thickness of the slab, and not the one affecting the width. Necking is a continuous process whose velocity depends on the vertical buoyancy forces acting on the slab and on the area of the section in which this force is applied, that results in extensional stresses. The necking rate increases due to two main reasons: weakening mechanisms for example, thermal diffusion, shear heating, grain size reduction, shear thinning (Bercovici et al., 2015; Schmalholz, 2011; Thielmann & Schmalholz, 2020); structural weakening (i.e., reduction of the thickness) (Schmalholz, 2011).
- *Slab break-off* occurs when the necking process locally reduces the thickness of the slab to $\sim$0. In our experiments, we define break-off to occur as soon as a portion of the slab reaches a thickness equal to 10% of its original thickness, which is approximately 1.5 cells along y direction. This cut-off is reasonable for the resolution that we employ.
- *Tearing* is the propagation of the break-off condition along the strike direction of the slab.

The three different concepts are illustrated in Figure 2. In Figure 2a, a large portion of the slab undergoes necking, with the western part being close to break-off. In Figure 2b, a horizontal tear is propagating along the strike of the slab from west to east.

In our numerical simulation, the necking processes is the effective cause of the break-off, and the tearing is the propagation of the break-off along strike. This diachronous breaking-off is a consequence of the pre-existent heterogeneity that affects the necking rate along strike. Based on these definitions, we divided the experiments in two main stages:

- *Necking stage*: This stage starts from the beginning of the numerical simulation and ends as soon as there is the first break-off. During this stage, the slab is necking and heating.
- *Tearing stage*: This stage starts as soon as the first break-off event is detected. This does not imply that the necking process, that started during the previous stage, stops but that its rate is affected by the tearing.

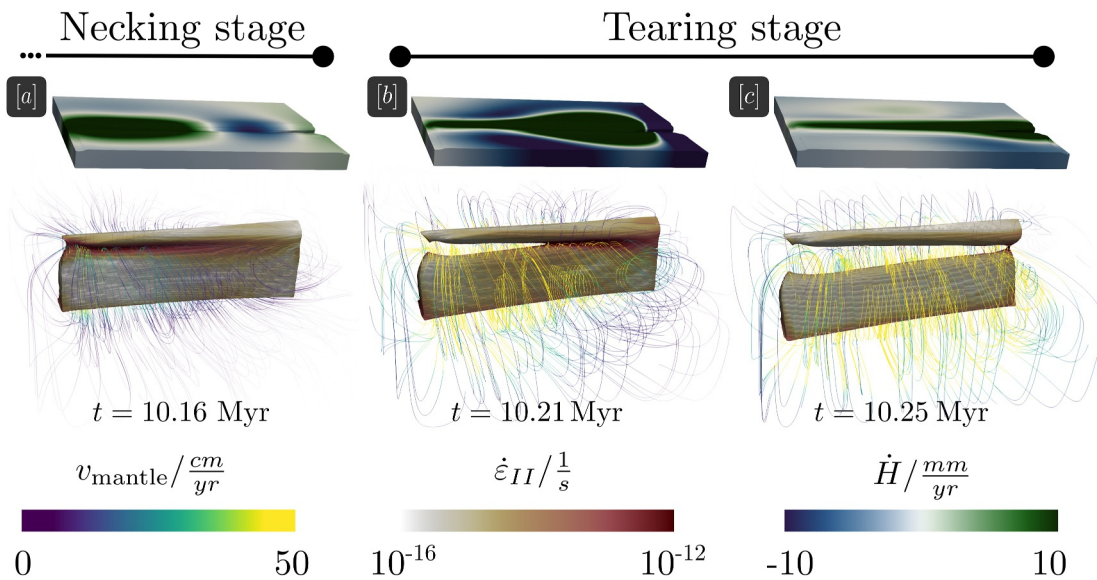


Figure 2. Fast tearing evolution. $v_s = 5\ \frac{\text{cm}}{\text{yr}}$, $V_{a,\text{dis}} = 8\ \frac{\text{cm}^3}{\text{mol}}$, $\tau_{\text{lim}} = 400$ MPa. We plot the slab, which is colored with the second invariant of the strain rate tensor ($\dot{\varepsilon}_{II}$) and the streamlines of the mantle velocity that are colored with velocity magnitude (v_{mantle}). On the top of the slab, we plot the crustal units colored with the surface velocities ($\dot{H}$).

To compute the tearing velocity, we use the time that is required to detach the segment between $100 - 1100$ km along the strike distance from West to East. $\dot{H}$ is monitored along the initial position of the slab (see Figure S4 in Supporting Information S1).

Figure S5 in Supporting Information S1 illustrates how the input parameters control the tearing velocity. The primary control is the activation volume, while the initial thermal structure has a second order. τ_{lim} has a third order control on the tearing velocity. We recognize two end member scenarios as a function of the tested parameters: fast and slow tearing.

3.1. Fast Tearing

In Figure 2, we show the general evolution of the fast tearing scenarios. Meanwhile in Figure 3 we plot the temporal evolution of $\dot{H}$, $D^{\dagger}$ and $\tau^{\dagger}_{\text{max}}$ along the strike of the slab. $D^{\dagger}$ is the thickness of the slab normalized with the initial thickness while $\tau^{\dagger}_{\text{max}}$ is the stress normalized with the τ_{lim}.

In the experiment shown in Figure 2 the necking stage lasts ~ 10 Myr, while the tearing stage lasts for ~ 0.14 Myr. During the necking stage, the deformation rate starts increasing in the portion of the slab where the highest amount of buoyant continental lithosphere is subducted (left Figure 2a). The tensional stress induced by the continental lithosphere subduction results in a localized necking instability. In the crustal section above the instability, we observe rapid uplift, $> 10\ \frac{\text{mm}}{\text{yr}}$ (see Figure 2a); meanwhile, the other portion of the crust is undergoing strong subsidence, $< -10\ \frac{\text{mm}}{\text{yr}}$. Figure 3a shows that there is a rapid decrease of stress where the necking instability develops while $\tau^{\dagger}_{\text{max}}$ increases in the other portion of the slab.

In the tearing stage, these processes continue generating a spatiotemporal pattern in the uplift. The stress increase in the still-attached portion of the slab promotes shear heating production that leads to slab weakening and a reduction of the pull stresses. The reduction of pull stresses increases uplift on top of the slab before its effective rupture (see Figures 2, 3b, and 3c). Throughout the migration of the tearing, we can observe that the orogen experiences a subsidence followed by a stronger uplift. During the initial stage, the uplift is $\sim 5\ \frac{\text{mm}}{\text{yr}}$ while the subsidence is $\sim -1\ \frac{\text{mm}}{\text{yr}}$. During the tearing stage, the uplift can be $\sim 56\ \frac{\text{mm}}{\text{yr}}$ while the subsidence in the still-attached portion of the slab is $\sim -16\ \frac{\text{mm}}{\text{yr}}$. After the tearing process, the uplift rapidly decreases, leaving the system quiescent.

21699356, 2026, 5, Downloaded from https://agupubs.onlinelibrary.wiley.com/doi/10.1029/2025JB032004 by Karlsruher Institut Fur Technologie, Wiley Online Library on [12/11/2026]. See the Terms and Conditions (https://onlinelibrary.wiley.com/terms-and-conditions) on Wiley Online Library for rules of use; OA articles are governed by the applicable Creative Commons License

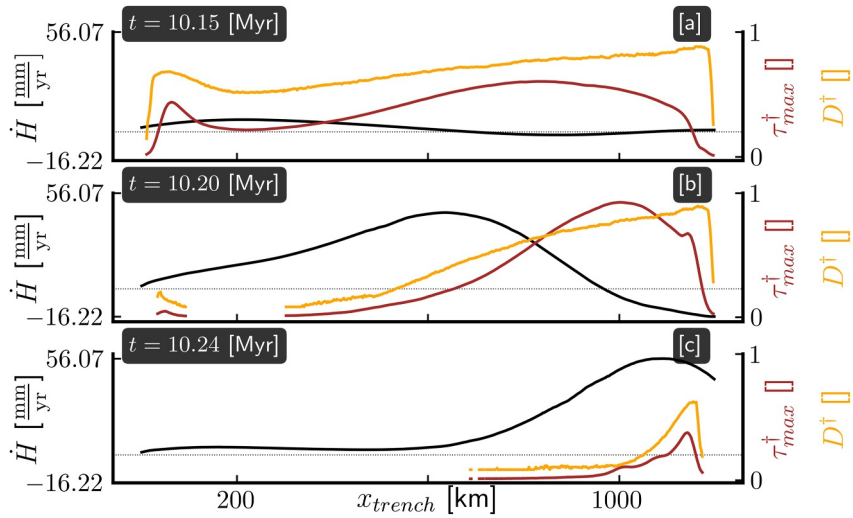


Figure 3. $\dot{H}$, $D^{\dagger}$ and $\tau_{\max}$ of the fast tearing end-member. Each plot represents one of the different timesteps shown in Figure 2. We collect the information of $\dot{H}$ along the strike of the slab, and it is plotted with a thick black line (left y-axis). $D^{\dagger}$ is the thickness normalized with the initial thickness D_0, while $\tau^{\dagger}_{\max}$ is the maximum stress normalized with $\tau_{\lim}$. $\tau^{\dagger}_{\max}$ and $D^{\dagger}$ are averaged values inside the necking zone, and they are plotted in brown and orange respectively (right y-axis). The necking zone is defined as a function of the minimum and maximum depth of detachment, see Table 2.

In Figure S6a in Supporting Information S1, we show the dominant deformation mechanisms during the necking stage, together with a representative section of the entire model along the y direction illustrating the effective viscosity. Throughout the experiment, deformation is primarily controlled by dislocation creep, whereas diffusion creep remains negligible and is confined to the uppermost part of the slab, where it coexists with localized plastic

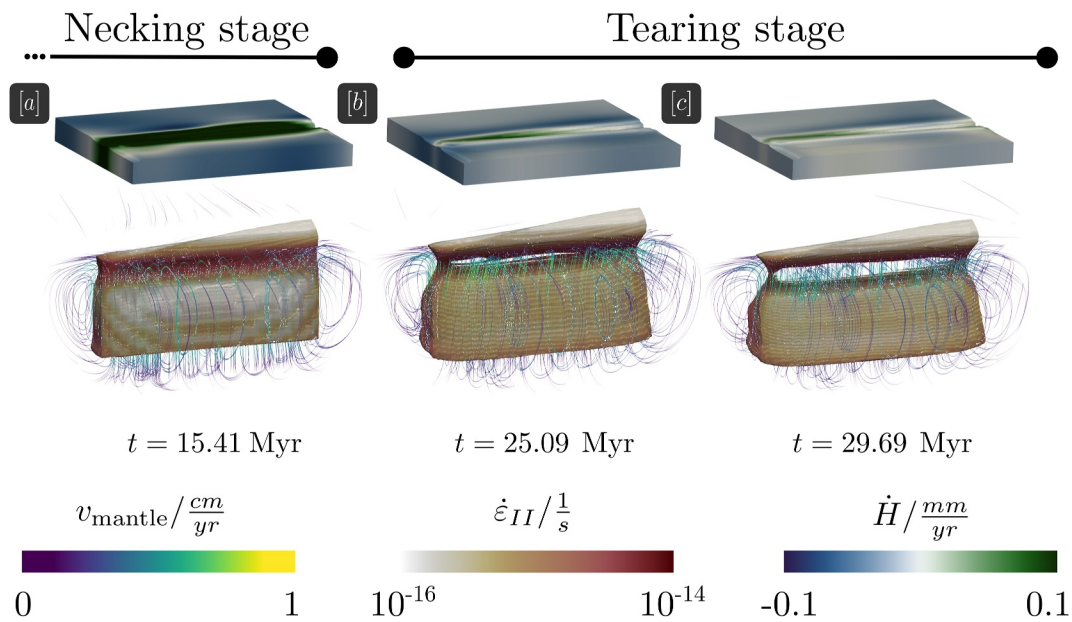


Figure 4. Slow tearing evolution. $v_s = 5$ $\frac{\text{cm}}{\text{yr}}$, $V_{a,\text{dis}} = 15$ $\frac{\text{cm}^3}{\text{mol}}$, $\tau_{\lim} = 400$ MPa. We plot the slab, which is colored with the second invariant of the strain rate tensor ($\dot{\varepsilon}_{II}$) and the streamlines of the mantle velocity that are colored with velocity magnitude (v_{mantle}). On the top of the slab, we plot the crustal units and we colored with the surface velocities ($\dot{H}$). The velocities reported both in the mantle and on the crustal unit are 2 order of magnitude less than in the fast tearing scenario (see Figure 2).

21699356, 2026, 5, Downloaded from https://agupubs.onlinelibrary.wiley.com/doi/10.1029/2025JB032004 by Karlsruher Institut Fur Technologie, Wiley Online Library on [12/11/2026]. See the Terms and Conditions (https://onlinelibrary.wiley.com/terms-and-conditions) on Wiley Online Library for rules of use; OA articles are governed by the applicable Creative Commons License

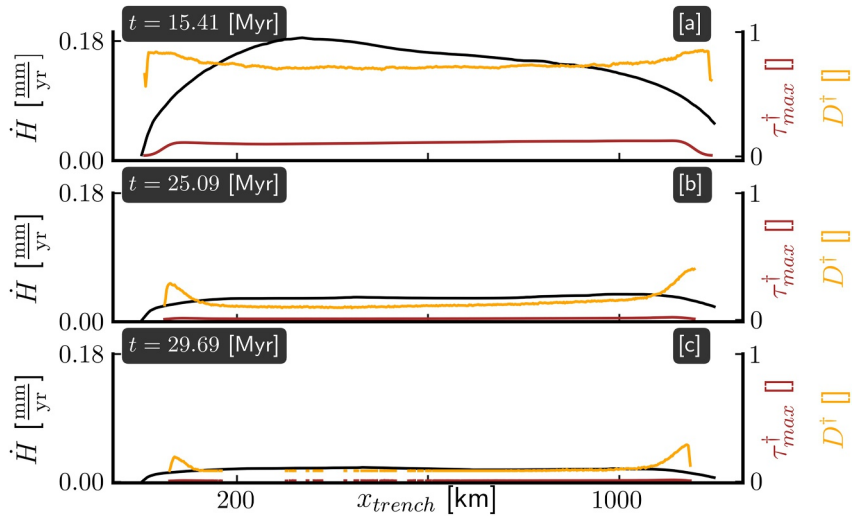


Figure 5. $\dot{H}$, $D^{\dagger}$ and $\tau_{\max}$ of the slow tearing end-member. Each plot correspond to the different timesteps shown in Figure 4. We collect the information of $\dot{H}$ along the strike of the slab, and it is plotted with a thick black line (left y-axis). $\tau^{\dagger}_{\max}$ and $D^{\dagger}$ are averaged values inside the necking zone, and they are plotted in brown and orange respectively (right y-axis). The necking zone is defined as a function of the minimum and maximum depth of detachment, see Table 2.

deformation. The stress limiter $\tau_{\lim}$ influences the overall stress magnitude; however, it becomes dominant mainly in the upper portion of the slab, where the lower temperature inhibits high deformation rates.

3.2. Slow Tearing

Figure 4 shows the evolution of the slow-tearing end-member scenario. The duration of the necking stage is significantly higher than the fast tearing scenario and can last more than 20 Myr before an effective break-off within the slab. As shown in Figure 4a, the slab necks almost homogeneously along the entire strike. The portion of the slab that experiences a slightly faster necking rate is below the portion of the plate where most of the continental lithosphere is subducted. During the necking stage, the uplift is small and mostly follows the pattern imposed by the collisional zone architecture. The tearing effectively starts after 25 Myr (see Figure 4b) and starts propagating from west to east (see Figure 5). The magnitude of uplift reaches its maximum during the necking stage at $\sim$0.2 $\frac{\text{mm}}{\text{yr}}$ and is negligible ($\sim$0.04 $\frac{\text{mm}}{\text{yr}}$) during the tearing stage (see Figure 5). The subsidence occurs mostly within the foreland basin.

In stark contrast with the fast tearing scenario, most of the uplift occurs during the necking stage before the tearing. In addition, the spatio-temporal pattern does not follow the stress evolution within the slab, but the pre-existing inherited structure (i.e., the subducted continental lithosphere).

For the fast-tearing scenario, Figure S6b in Supporting Information S1 shows the dominant irreversible deformation mechanisms together with a representative section of the effective viscosity along the y direction. Similar to the previous case, deformation is predominantly accommodated by dislocation creep, whereas diffusion creep and plastic deformation are restricted to the uppermost part of the slab.

3.3. Cumulative Topography Variation

In Figure 6, we plot the cumulative topography variation of the necking and tearing stage, and the long-term topography variation (the entire simulation) of both the fast and slow tearing end-member scenarios. We compute the average surface velocities along x_{trench}, which is the strike of the midplane of the slab (black tick line in the plots in Figure 6), and collect these value in Table 2.

In the case of fast tearing, the total cumulative uplift and subsidence during the necking stage is $\sim$2000 and ~ -1200 m respectively, which corresponds to an average surface velocity along x_{trench} of 0.034 $\frac{\text{mm}}{\text{yr}}$ (see Table 2, $\dot{H}_N$). During the tearing stage, the average surface velocity along x_{trench} is 17 $\frac{\text{mm}}{\text{yr}}$ (see Table 2, $\dot{H}_{Te}$).

21699356, 2026, 5, Downloaded from https://agupubs.onlinelibrary.wiley.com/doi/10.1029/2025JB032004 by Karlsruher Institut Fur Technologie, Wiley Online Library on [12/11/2026]. See the Terms and Conditions (https://onlinelibrary.wiley.com/terms-and-conditions) on Wiley Online Library for rules of use; OA articles are governed by the applicable Creative Commons License

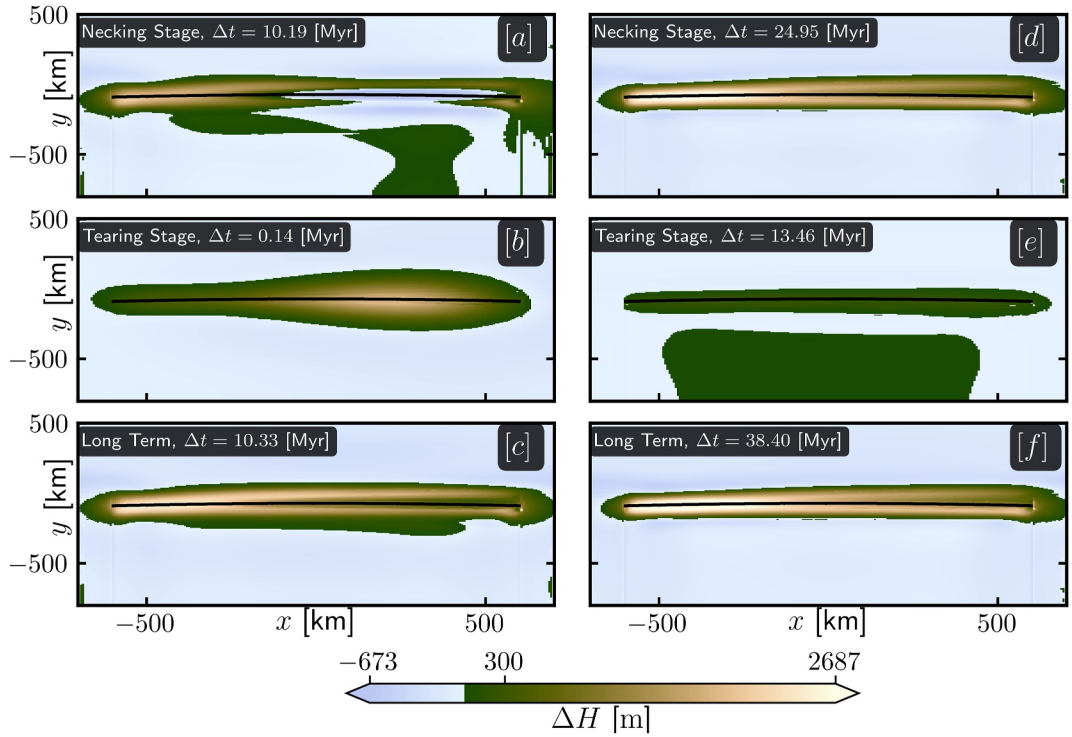


Figure 6. Cumulative topography variation. (a–c) Fast Tearing cumulative topography variation (ΔH). (d–f) Slow tearing cumulative topography variation. The thick black lines represent the initial position of the slab. Each row of figures represent a different stage of the experiments: 1st row: necking stage; 2nd: tearing stage; 3rd: the entire cumulative topography variation.

In the slow tearing scenario, the total surface velocity has no clear spatial pattern, and, in particular, subsidence is negligible and confined in the rims of the orogen (see Figure 6b). Figure 6d shows that most of the cumulative topography variation (whose maximum is ∼3000 m) occurs in the leftmost portion of the collisional zone. Most of the topography variation occurs during the necking stage (see Figure 6e). The average surface velocity along

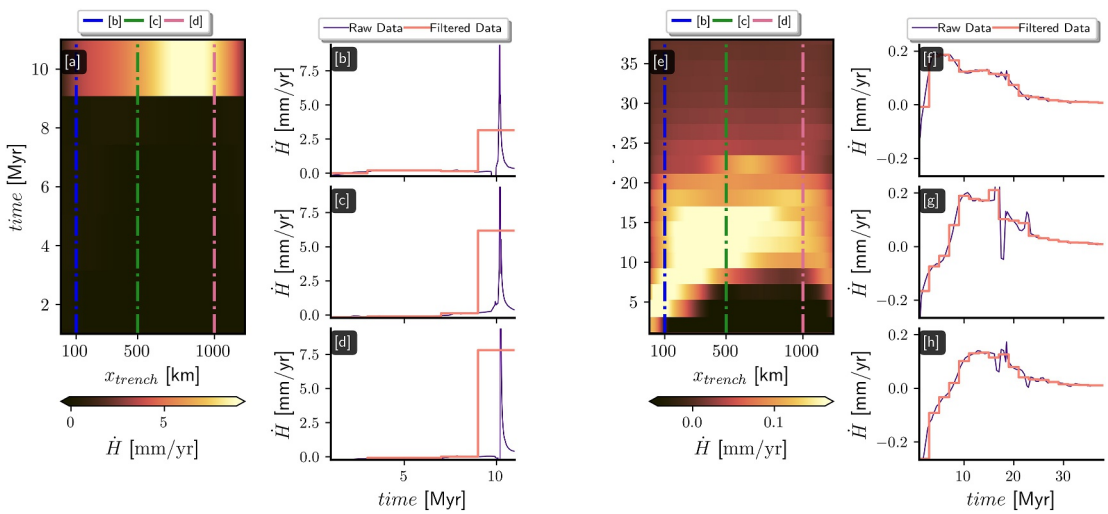


Figure 7. Surface velocities and time resolution: (a–d): Fast tearing; (e–h): Slow tearing. (a) and (e): Heat maps representing the surface velocities evolution in the low time resolution data. The *x*-axis represents the distance along the trench, and *y*-axis the time. In each plot, we highlight the points that are tracked in the profiles (b)–(d) and (f)–(h). (b)–(d) & (f)–(h): Time evolution of three specific points along the trench. *x*-axis represents the time, and *y*-axis the surface velocities: the red thick lines represent the low time resolution data set, while the purple lines represent the instantaneous surface velocities.

21699356, 2026, 5, Downloaded from https://agupubs.onlinelibrary.wiley.com/doi/10.1029/2025JB032004 by Karlsruher Institut Fur Technologie, Wiley Online Library on [12/11/2026]. See the Terms and Conditions (https://onlinelibrary.wiley.com/terms-and-conditions) on Wiley Online Library for rules of use; OA articles are governed by the applicable Creative Commons License

Table 2
Experiment Table

Test name	v_s ($\frac{cm}{yr}$)	$\bar{T}$ (°C)	τ_{lim} (MPa)	$V_{a,dis}$ ($\frac{cm^3}{mol}$)	$v_{tearing}$ ($\frac{cm}{yr}$)	$\dot{H}_N$ ($\frac{mm}{yr}$)	$\dot{H}_{Te}$ ($\frac{mm}{yr}$)	$\dot{H}_{LT}$ ($\frac{mm}{yr}$)	$d_{tearing}$ (km)
TSD2PR	5.0	846.200	200	8	2600	0.088	37	0.410	−125.900 ± 18.531
TSD2V10PR	5.0	846.200	200	10	460	0.093	5.800	0.270	−132.300 ± 12.784
TSD2V13PR	5.0	846.200	200	13	69	0.120	0.310	0.140	−150.900 ± 17.438
TSD2V15PR	5.0	846.200	200	15	8.100	0.080	0.019	0.059	−146.200 ± 10.954
TSD3PR	10	807.800	200	8	5400	0.110	83	0.570	−125.200 ± 12.770
TSD3V10PR	10	807.800	200	10	890	0.087	12	0.310	−128.700 ± 11.516
TSD3V13PR	10	807.800	200	13	76	0.100	0.440	0.130	−145.200 ± 11.501
TSD3V15PR	10	807.800	200	15	11	0.073	0.020	0.059	−145.400 ± 7.788
TSD4PR	2.5	900.300	200	8	530	0.037	7.300	0.300	−142.600 ± 20.050
TSD4V10PR	2.5	900.300	200	10	340	0.100	3.100	0.230	−149.200 ± 11.778
TSD4V13PR	2.5	900.300	200	13	36	0.140	0.130	0.140	−158.500 ± 27.399
TSD4V15PR	2.5	900.300	200	15	5.900	0.088	0.016	0.054	−151.500 ± 21.637
TSD2PR2	5.0	846.200	600	8	1500	0.024	16	0.150	−146.100 ± 16.103
TSD2V10PR2	5.0	846.200	600	10	650	0.075	4.300	0.140	−147.800 ± 9.974
TSD2V13PR2	5.0	846.200	600	13	58	0.110	0.200	0.130	−152.300 ± 17.348
TSD2V15PR2	5.0	846.200	600	15	8.700	0.079	0.018	0.059	−147 ± 10.438
TSD3PR2	10	807.800	600	8	1700	0.032	19	0.130	−145.200 ± 15.733
TSD3V10PR2	10	807.800	600	10	750	0.068	5.100	0.130	−147 ± 10.669
TSD3V13PR2	10	807.800	600	13	78	0.100	0.230	0.110	−151.400 ± 8.581
TSD3V15PR2	10	807.800	600	15	13	0.070	0.020	0.060	−147.500 ± 6.347
TSD4PR2	2.5	900.300	600	8	860	0.027	9.200	0.200	−152.100 ± 19.156
TSD4V10PR2	2.5	900.300	600	10	450	0.096	3.300	0.200	−154 ± 10.077
TSD4V13PR2	2.5	900.300	600	13	43	0.140	0.130	0.140	−159.700 ± 25.952
TSD4V15PR2	2.5	900.300	600	15	6.700	0.090	0.017	0.057	−152.200 ± 22.061
TSD2	5.0	846.200	400	8	1600	0.034	17	0.150	−144.900 ± 13.482
TSD2V10	5.0	846.200	400	10	660	0.079	4.600	0.150	−147.200 ± 10.316
TSD2V11	5.0	846.200	400	11	320	0.084	2.100	0.150	−150.100 ± 10.522
TSD2V12	5.0	846.200	400	12	210	0.100	0.820	0.140	−149.600 ± 8.658
TSD2V13	5.0	846.200	400	13	59	0.100	0.240	0.120	−154.400 ± 17.407
TSD2V15	5.0	846.200	400	15	7.700	0.079	0.018	0.057	−147.100 ± 11.130
TSD3	10	807.800	400	8	2300	0.036	22	0.130	−143.800 ± 10.319
TSD3V10	10	807.800	400	10	650	0.054	5.400	0.130	−146.100 ± 6.829
TSD3V11	10	807.800	400	11	360	0.077	2.400	0.130	−148 ± 9.707
TSD3V12	10	807.800	400	12	230	0.088	0.930	0.120	−148.700 ± 6.394
TSD3V13	10	807.800	400	13	77	0.100	0.240	0.110	−151.600 ± 8.990
TSD3V15	10	807.800	400	15	14	0.069	0.020	0.059	−146.300 ± 6.336
TSD4	2.5	900.300	400	8	840	0.023	9.300	0.200	−150.700 ± 16.879
TSD4V10	2.5	900.300	400	10	450	0.088	3.300	0.190	−153.200 ± 12.149
TSD4V11	2.5	900.300	400	11	270	0.130	1.300	0.190	−155 ± 9.984
TSD4V12	2.5	900.300	400	12	120	0.130	0.520	0.170	−155.400 ± 18.355
TSD4V13	2.5	900.300	400	13	34	0.130	0.150	0.140	−160 ± 25.685
TSD4V15	2.5	900.300	400	15	6.500	0.089	0.017	0.056	−152.100 ± 22.760

Note. The two bold experiments are the reference scenarios showed in Figures 2 and 4. In this table we introduce: $\bar{T}$ the average temperature of the slab at 100 km of depth; $\dot{H}_{Ne|Te|LT}$ that are surface velocities for the necking, tearing stages and for the entire simulation respectively.

21699356, 2026, 5, Downloaded from https://agupubs.onlinelibrary.wiley.com/doi/10.1029/2025JB032004 by Karlsruher Institut Fur Technologie, Wiley Online Library on [12/11/2026]. See the Terms and Conditions (https://onlinelibrary.wiley.com/terms-and-conditions) on Wiley Online Library for rules of use; OA articles are governed by the applicable Creative Commons License

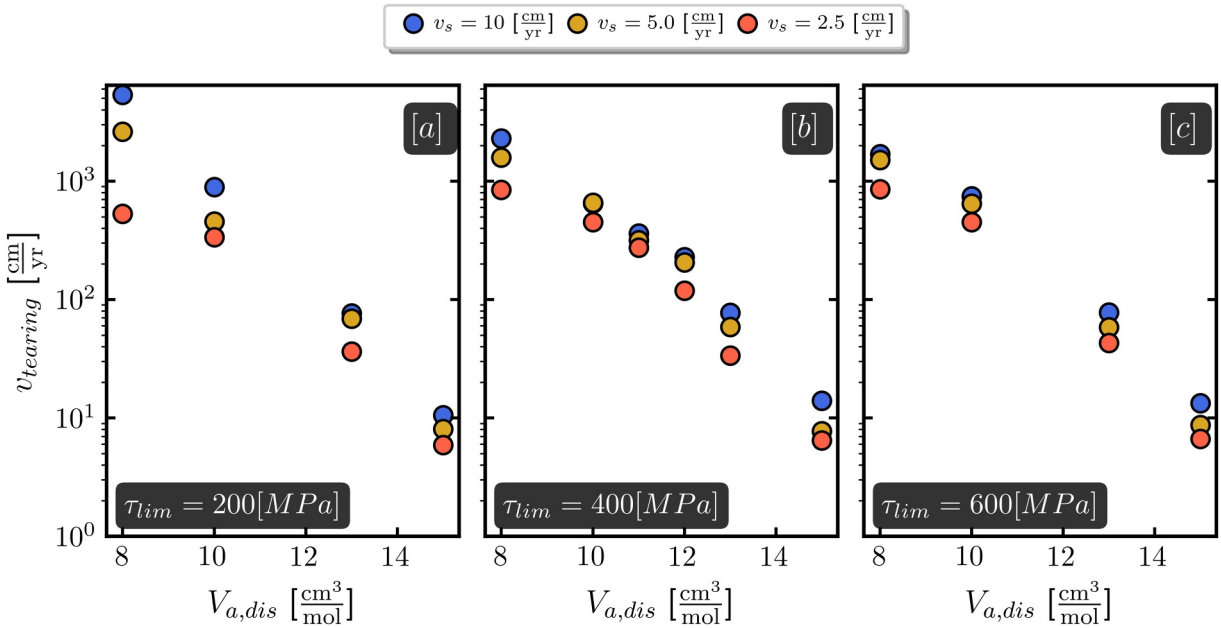


Figure 8. Effect of the pressure dependence of the mantle viscosity on the tearing velocity. *x* axis is the activation volume, the *y* axis is the tearing velocity (the axis is in $\log_{10}$ scale). Each colored dot represents a different experiment. They are colored accordingly to their initial v_s, see, in addition, Figure S5 in Supporting Information S1.

x_{trench} is ∼0.08 and ∼0.02 $\frac{mm}{yr}$ respectively for the necking and tearing stage of the slow tearing scenario. Long-term cumulative topography variation is similar for fast and slow tearing (Figures 6e and 6f).

3.4. Instantaneous Surface Velocites and Time Resolution

We track the instantaneous surface velocities along the strike of the mid plane of the slab (see Figures 3 and 5). We observe several orders of magnitude difference during the evolution of the numerical experiments with surface velocities that can achieve values up to 80 $\frac{mm}{yr}$. However, the estimated surface velocity determined by geochronology and GPS data are average quantities over larger time intervals (e.g., Fox et al., 2016). To extract information that is comparable with the geological record, it is necessary to down-sample our the data.

We follow the maximum time resolution possible from the study of Fox et al. (2016) (i.e., 2 Myr). We average the value of $\dot{H}$ along the initial position of the slab using 2 Myr windows, starting at 1 Myr. This prevents the data being affected by the initial isostatic rebound typical of any geodynamic models (Spang et al., 2021). In Figure 7, we plot the results for the tests shown in Figures 2 and 4. Meanwhile in Figures S7–S10 of the Supporting Information S1 we plot the entire suite of experiments featuring τ_{lim} = 200 MPa and v_s = 5 $\frac{cm}{yr}$.

In Figure 7a, we plot the downsampled surface velocity profile of the fast tearing scenario (see Figures 2 and 3). The averaged uplift ranges from 0.05 to 8 $\frac{mm}{yr}$ while the real uplift in the unprocessed data reaches values up to 17 $\frac{mm}{yr}$ (see Table 2 [*TSD2*]). The tearing event occurs between 9 and 11 Myr. Within this time window, the uplift suddenly grows and reaches its peak toward the tearing propagation direction. In Figures 7b–7d we plot three representative 0*D* profiles taken at 100, 500, and 1,000 km along x_{trench}. We plot the downsampled uplift and the original results. The original data indicate that the uplift associated with tearing is an impulsive process that decays exponentially. There is a temporal shift between the peaks as a function of the x_{trench}.

In Figure 7e, we plot the downsampled surface velocity of the slow tearing scenario. First, the magnitude of the uplift is $\sim 0.1 - 0.2$ $\frac{mm}{yr}$ in both the raw and downsampled data. Second, the uplift peak that is observed during the necking stage migrates without a tearing process.

The surface velocity signal is decreasing as a function of the activation volume, while its timing is increasing. Tearing signal becomes almost invisible when the mantle is not effectively shear thinning during the break-off and tearing processes as can be seen in Figures S7–S10 of the Supporting Information S1.

21699356, 2026, 5, Downloaded from https://agupubs.onlinelibrary.wiley.com/doi/10.1029/2025JB032004 by Karlsruher Institut Fur Technologie, Wiley Online Library on [12/11/2026]. See the Terms and Conditions (https://onlinelibrary.wiley.com/terms-and-conditions) on Wiley Online Library for rules of use; OA articles are governed by the applicable Creative Commons License

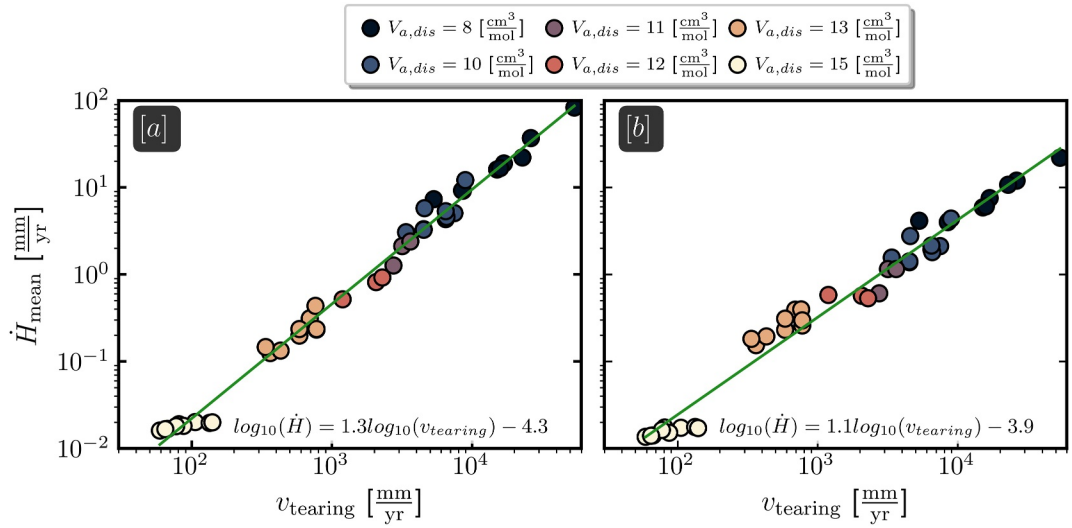


Figure 9. Tearing velocity and mean surface velocity. Each point represents an experiment. They are colored accordingly to the activation volume of the dislocation creep of the mantle. The axis are both in $\log_{10}$ scale. The green lines are the results of the linear regression of the data point. (a): Unprocessed data; (b): Poor temporally resolved data.

3.5. Tearing Velocity and Surface Velocities

In Figure 8 (and Figure S5 in Supporting Information S1), we plot the average tearing velocity against the dislocation creep activation volume of the mantle, which controls the average viscosity of the mantle along the slab. Each subplot represents a different τ_{lim} while the different colors refer to the convergence velocity used to describe the slab's thermal structure.

The activation volume of the mantle has a first-order control over the system and controls the tearing velocity. We do not observe abrupt changes of the tearing regime (see Figure S5 in Supporting Information S1). The tearing velocity gradually changes as a function of the dislocation creep activation volume. $V_{a,dis}$ controls the average viscosity of the mantle along the slab and the propensity of the mantle to shear thinning during the detachment processes. If the dominance of dislocation creep over diffusion creep decreases, drag forces start acting against the tearing, thereby reducing the stresses within the slab. This occurs due to the thermal assimilation of the slab into the upper mantle. If the timescales of the tearing and necking are increased, thermal diffusive processes start becoming significant and reduce the impact of the prescribed initial conditions.

τ_{lim}, the maximum stress bearable by the slab and v_s, the average subduction velocity prior the subduction, have a second-order effect that is only apparent for low mantle activation volumes. τ_{lim} has a second order effect because when the $V_{a,dis}$ is sufficiently high, the stress within the slab cannot grow significantly during the breaking-off process. τ_{lim} has a significant impact on the depth of tearing, as shown in Figure S11 of the Supporting Information S1. The initial thermal structure has a second-order effect, we observe that hotter slabs (low v_s) feature the slowest tearing velocity (see Figure 8).

In Figure 9a, we plot $v_{tearing}$ against the average $\dot{H}$ along the initial position of the slab. The two quantities are strongly correlated, indicating that the average surface velocity is proportional to the tearing velocity. We additionally compute the linear regression of this data set, yielding a linear relation that connect the $\log_{10}(v_{tearing})$ and $\log_{10}(\dot{H})$ (both in $\frac{mm}{yr}$). This linear relation has an R^2 of 0.99 and a standard error on the intercept and slope of 0.05 and 0.02 respectively. In Figure 9b, we plot the average uplift velocity using the low time resolution post-processed data. It is consistent with the raw data.

The style of tearing critically depends on the ability of the mantle to accommodate the detachment and tearing processes. If the mantle is not weak enough during the necking stage, the slab loses its negative buoyancy due to the thermal diffusion and its internal stresses cannot grow. This will be reflected in the uplift history of the orogen, indicating that slab tearing processes cannot be properly detected if the mantle has sufficient strength to oppose the necking instability. In addition, if the slab break-off and consequent tearing are inhibited the spatio-temporal

21699356, 2026, 5, Downloaded from https://agupubs.onlinelibrary.wiley.com/doi/10.1029/2025JB032004 by Karlsruher Institut Fur Technologie, Wiley Online Library on [12/11/2026]. See the Terms and Conditions (https://onlinelibrary.wiley.com/terms-and-conditions) on Wiley Online Library for rules of use; OA articles are governed by the applicable Creative Commons License

21699356, 2026, 5, Downloaded from https://agupubs.onlinelibrary.wiley.com/doi/10.1029/2025JB032004 by Karlsruher Institut Fur Technologie, Wiley Online Library on [12/11/2026]. See the Terms and Conditions (https://onlinelibrary.wiley.com/terms-and-conditions) on Wiley Online Library for rules of use; OA articles are governed by the applicable Creative Commons License

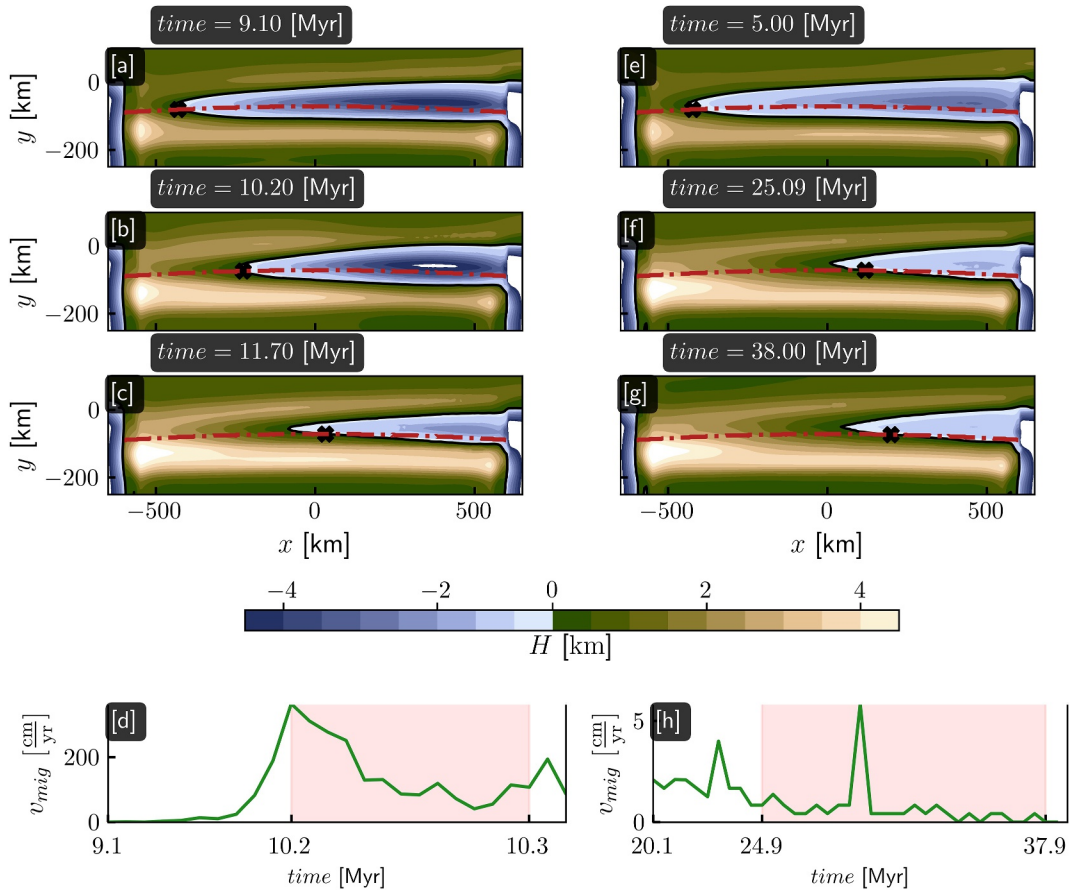


Figure 10. Shoreline migration. (a)–(f): Topography evolution of the two end member scenarios: left column, fast tearing end member; right column, slow tearing end member. The red dashed lines represent the initial position of the slab (x_{trench}), the black thick markers represent the position of the shoreline. (d), (h): Migration of the shoreline versus time. The green thick line represent the velocity with which the shoreline is migrating along strike. The red shaded area highlight the time frame in which the slab tearing is occurring.

fingerprint of tearing becomes weak and undistinguishable from the surface velocities imposed by the along strike compositional variation.

We analyze the average tearing depth (d_{tearing}) (see Figure S11 in Supporting Information S1) with respect to the input data. The sensitivity of d_{tearing} to the activation volume and the sinking velocity critically depends on τ_{lim}. For $\tau_{\text{lim}} = 200$ MPa, we observe a systematic increase in d_{tearing} as a function of $V_{a,\text{dis}}$, ranging from -120 km to -160 km. In contrast, for $\tau_{\text{lim}} \geq 400$ MPa, the depth's dependence on the mantle's activation volume is minimal (approximately 20 km), and the average depth of tearing remains within -140 km to -160 km across all experiments. Notably, the greatest depth of tearing is associated with experiments involving the lowest sinking velocity, which corresponds to the warmest slab.

4. Discussion

4.1. Summary of Results

Most of our results show that mantle rheology plays a crucial role in determining the style of tearing and detachment. We show that, depending on the mantle's rheology, stress build-up within the slab can be limited, thereby affecting tearing and uplift velocities. We describe two end-member scenarios: fast and slow tearing. These end-members differ in the timescales of the uplift, but they yield similar cumulative topographic variation. We show the correlation between uplift and tearing velocities: the average surface velocity is positively correlated

21699356, 2026, 5, Downloaded from https://agupubs.onlinelibrary.wiley.com/doi/10.1029/2025JB032004 by Karlsruher Institut Fur Technologie, Wiley Online Library on [12/11/2026]. See the Terms and Conditions (https://onlinelibrary.wiley.com/terms-and-conditions) on Wiley Online Library for rules of use; OA articles are governed by the applicable Creative Commons License

with the tearing velocity. Moreover, we show how the surface signals can become weak as a function of the viscosity of the mantle.

We incorporate shear heating as a weakening mechanism in our models. Shear heating (Ψ) plays a significant role in fast tearing scenarios (see Figure S12 in Supporting Information S1). As demonstrated in our numerical experiments (Figures 2 and 3), shear heating locally increases temperature, reducing slab viscosity and accelerating the necking process. However, shear heating becomes negligible in slow tearing scenarios because both the necking rate and stress accumulation within the slab are inhibited by mantle drag forces. This indicates that weakening mechanisms reliant on energy dissipation are strongly influenced by mantle rheology. If the viscosity of the surrounding mantle does not weaken more rapidly than the slab itself, shear heating remains ineffective. For further insights, we invite the reader to view Movies S1–S3.

4.2. Comparison With Previous Work

Our systematic studies show a wide range of v_{tearing} and corresponding surface velocities compared to other works. Tearing velocities range from $\sim$6 to 5400 $\frac{\text{cm}}{\text{yr}}$, while surface velocities ($\dot{H}$) vary from $\sim$0.01 to $\sim$80 $\frac{\text{mm}}{\text{yr}}$ (or from $\sim$0.1 to 21.0 $\frac{\text{mm}}{\text{yr}}$ using the downsample data set). The variability in our results stems from mantle rheology, which, according to our findings, exerts a first-order control on the dynamics of slab break-off and tearing. Previous 3D numerical studies have obtained tearing velocities ranging from $\sim$10 to 160 $\frac{\text{cm}}{\text{yr}}$ (Andrić-Tomašević et al., 2023; Boonma et al., 2023; Burkett & Billen, 2010; Duretz et al., 2014; Maiti et al., 2024; van Hunen & Allen, 2011).

Direct comparison with these studies is not straightforward, as differences in initial setup, geometry, and modeling choices can significantly affect tearing velocities and surface velocities. The initial geometry, numerical domain size, and boundary conditions can influence the results. For example, van Hunen and Allen (2011), Duretz et al. (2014), and Capitanio and Replumaz (2013) investigate tearing processes starting from a pre-collisional stage, where the slab interacts with the lower boundary of the numerical domain. This interaction can alter tearing velocities by introducing an additional force opposing buoyancy. Thus, despite using either no activation volume or lower values than in our experiments, the authors obtain similar results due to the interaction with the transition zone and the lower boundary of the numerical domain. The collisional stage introduces realistic heterogeneities and helps produce a self-consistent temperature structure of the descending plate. For instance, in their models, a relationship is observed between convergence velocity and break-off depth (Duretz et al., 2012, 2014), whereas in our experiments, such high variability in detachment and tearing depth is not evident (see Figure S11 in Supporting Information S1).

Differences may also arise from the geological setting under investigation. For example, Burkett and Billen (2010) explore the effects of ridge subduction interactions, considering a warmer and weaker slab than in our baseline scenarios. The initial subduction and collisional configurations play a crucial role in the models of Andrić-Tomašević et al. (2023) and Maiti et al. (2024), where the authors vary the passive margin angle relative to the subducting plate. This configuration has several consequences: (a) it imposes a strong along-strike variation in the subducting plate; (b) it introduces an additional time-dependent source of extensional stress on the slab, which depends on the angle between the subduction trench and the passive margin. In both studies, a systematic decrease in tearing velocity is observed as a function of the passive margin angle. This is a direct consequence of the imposed kinematic-dynamic boundary conditions and the collisional zone configuration, which effectively control the resistive forces along the slab strike and, consequently, the necking rate.

The rheological model further influences the results by introducing additional weakening mechanisms in the slab due to deformation rate-dependent effects (e.g., grain-size reduction). Nevertheless, the studies by Andrić-Tomašević et al. (2023), Maiti et al. (2024), and Boonma et al. (2023), which incorporate grain-size reduction, are consistent with our intermediate scenarios and yield similar tearing behavior.

The average uplift velocities we report are similar to those of Duretz et al. (2011, 2014), and Boonma et al. (2023) ($\sim 0.8 - 2.5$ $\frac{\text{mm}}{\text{yr}}$). In contrast, Maiti et al. (2024) report uplift rates ranging from 4 to 15 $\frac{\text{mm}}{\text{yr}}$. If we use the linear equations shown in Figure 9 and input the tearing velocities predicted by previous numerical studies (see Maiti et al. (2024) for a complete data compilation), the resulting surface velocities $\dot{H}$ values are below 1 $\frac{\text{mm}}{\text{yr}}$, whereas the estimated values in their models exceed 10 $\frac{\text{mm}}{\text{yr}}$. A direct comparison remains challenging due to differences in

21699356, 2026, 5, Downloaded from https://agupubs.onlinelibrary.wiley.com/doi/10.1029/2025JB032004 by Karlsruher Institut Fur Technologie, Wiley Online Library on [12/11/2026]. See the Terms and Conditions (https://onlinelibrary.wiley.com/terms-and-conditions) on Wiley Online Library for rules of use; OA articles are governed by the applicable Creative Commons License

the employed rheological model. However, it is likely that their mantle viscosity is significantly weakened due to grain-size reduction.

4.3. Comparison With Natural Cases

Our numerical models are designed to study tearing velocities and surface velocity signals. Therefore, we selected geological cases where such data are available or can be reasonably estimated. Surface deformation in nature may be the result of different underlying processes. For example, the architecture of sedimentary basins and the migration of depocenters can be linked to continent-continent collisions or deep mantle processes (L. H. Eskens et al., 2024; Kuhlemann, 2007; Meulenkamp et al., 1996; Schlunegger & Kissling, 2015). Additionally, estimates of paleoelevation (Schildgen et al., 2014) and past-to-recent denudation/exhumation rates (Fox et al., 2016; Sternai et al., 2019) have been used to infer deep mantle processes. The migration of volcanic activity (Ferrari, 2004) has also been analyzed to study slab dynamics. While various geological processes can explain these data (see Garzanti et al. (2018) for further discussion), we assume that these signals are primarily related to slab break-off and tearing and discuss them in relation to our results. We stress that the geological history of orogens cannot be represented by these numbers. The comparison is intended only to show how closely our results resemble natural examples and how our modeling insights can aid the interpretation of geological data.

Several studies have attempted to estimate tearing velocities in different geological settings. For example, Ferrari (2004) proposed a lateral propagation of slab break-off beneath the Trans-Mexican Volcanic Belt, from the Gulf of California to the Gulf of Mexico (12–6 Ma), inferred from short-lived mafic volcanic pulses. Based on these data, Ferrari (2004) estimated a tearing velocity of 25 $\frac{cm}{yr}$ from 12 to 10 Ma and 10 $\frac{cm}{yr}$ from 10 to 6 Ma. Ascione et al. (2012) analyzed the evolution of wedge-top sedimentary sequences in the southern Apennines thrust belt and observed a systematic southeastward migration of depocenters, with an estimated migration rate of 10–14 $\frac{mm}{yr}$ from 4 to 2.8 Ma, which the authors attributed to lateral tearing. Similarly, Cosentino et al. (2012) and Schildgen et al. (2014) studied the tectonic history of the Anatolian Plateau. The authors interpreted the east-to-southwest migration of uplift (10–5 Ma) as a result of lateral slab break-off, estimating a migration rate of 10–17 $\frac{mm}{yr}$. Meulenkamp et al. (1996) used stratigraphic data to calculate the migration rate of sedimentary depocenters along the East Alps–Carpathian orogenic system. The eastward migration of foreland basin depocenters occurred between 27 and 11 Ma along an arcuate orogen of 1600 km. The authors identified four distinct migration rates:

- 5.5 $\frac{cm}{yr}$ (27–17.5 Ma);
- 13.5 $\frac{cm}{yr}$ (17.5–16.5 Ma);
- 45 $\frac{cm}{yr}$ (16.5–15.5 Ma);
- 13 $\frac{cm}{yr}$ (15.5–11.5 Ma).

The average velocity of depocenter migration is 10 $\frac{cm}{yr}$. If these values represent effective tearing velocities, slow-tearing scenarios best align with natural data. For instance, tearing velocities over time (see Figure S13f in Supporting Information S1) show a pattern similar to the lateral migration of the Alps–Carpathian system.

The tearing velocities estimations are consistent with our slow-tearing scenarios. However, this agreement is problematic. Slow-tearing scenarios exhibit average velocities ranging from 5 to 20 $\frac{cm}{yr}$ but do not display tearing-induced surface velocities patterns. As shown in Figure 7, uplift and subsidence in slow-tearing cases primarily result from the compositional differences in subducted material along strike. Additionally, most foreland-basin uplift occurs during the necking stage. Thus, while our results align with natural observations, they also suggest that slab break-off and tearing may not produce detectable surface signals (see Figure 9).

To address this issue, we must either refute slab break-off and tearing as primary drivers of the diachronic evolution of several basins or reconsider what we measure and how geological data compare with our numerical results. We begin with a thought experiment. Sedimentological processes depend on factors such as climate, rock erodibility, and topography. Sedimentary facies primarily depend on depositional settings, which in turn are controlled by the relative position of the depositional surface to sea level. Therefore, shoreline migration can serve as a proxy for estimating the rate at which sedimentary facies migrate in response to tearing. We acknowledge that other processes, such as eustasy, variations in sediment supply induced by changes in precipitation rates, or differences in erodibility, can lead to shoreline migration. However, these factors typically operate on short time scales (~0.5–1 million years), are local and many exhibit cyclic variations (e.g., Forte et al., 2016; Haq

et al., 1988; Leeder et al., 1998). Consequently, we do not expect these processes to impact the long-term shoreline migration controlled by slab tearing, which is predominantly one-directional. L. Eskens et al. (2025) recently demonstrated that slab break-off processes predominantly influence sedimentary basin architecture over eustacy on the longer time scale.

In Figure 10 (and Figure S14 in Supporting Information S1), we plot shoreline migration along for different experiments featuring different mantle activation volumes. Our main observations are as follows:

1. Shoreline migration and surface velocities begin before tearing.
2. In most cases, shoreline migration velocity is an order of magnitude lower than tearing velocity (see Figures S13 and S14 in Supporting Information S1).
3. Surface signals become negligible after the tearing process.

If we apply these observations to real-world scenarios, we hypothesize that the diachronic evolution of a basin provides only a minimal estimate of tearing velocities and that surface velocities primarily results from slab yielding before effective tearing. Similar inconsistencies between natural and modeled data can be seen in uplift/exhumation data. For instance, uplift associated with the Anatolian Plateau (Schildgen et al., 2014) is approximately 0.7 $\frac{\text{mm}}{\text{yr}}$, aligning with intermediate tearing scenarios (see Figure 9; Figures S6–S9 in Supporting Information S1). However, our numerical simulations suggest that such uplift rates would imply tearing velocities ranging from 80 to 400 $\frac{\text{cm}}{\text{yr}}$.

These findings highlight the need for a numerical framework that integrates sedimentological and geodynamic processes. Geological data retrieved from numerical simulations cannot be directly mapped onto available natural data. Therefore, it is crucial to understand: (a) how geological records respond to deep mantle processes, and (b) how external factors (e.g., eustatic cycles, local climate) contribute to modifying geological signals.

4.4. Limitations

Our baseline scenario is a simplified collisional zone after the convergence fades. We do not account for the collisional history, which might play a role in shaping the detachment process (Ribe & Xu, 2020). This prevents us from having a realistic geotherm and rheological state of the crust, the latter, in particular, might play a role in the lithospheric dynamics (Magni et al., 2013). In addition, we do not investigate the role of the length of the slab, nor do we study how tearing velocity can be shaped by the interaction between the slab and the transition zone.

We do not employ grain size reduction or LTP. Grain size reduction and low-temperature plasticity can reduce the viscosity of the slab and/or mantle (Bellas et al., 2018; Bercovici et al., 2015, 2019; Thielmann & Schmalholz, 2020). As a function of the activation volume, the stress required to activate LTP cannot be reached during the necking process (Spang et al., 2024). This has been partially confirmed by our results in which τ_{lim} is not reached for $V_{a,\text{dis}}$ higher than 10 $\frac{\text{cm}^3}{\text{mol}}$. Grain size reduction depends on how the dissipative energy of deformation is partitioned between shear heating and mechanical work (Thielmann, 2018; Thielmann & Schmalholz, 2020). In particular, we cannot quantify how much the grain-size affects the mantle weakening and what the trade-off with the other rheological parameters are.

We focus on the post-collisional evolution; however, the preceding collisional history strongly influences the rheological structure of the orogen (Faccenda et al., 2008; Menant et al., 2016; Piccolo et al., 2018). For example, hot orogens such as the Himalaya (Beaumont et al., 2001) are largely dominated by gravitational collapse. If tearing processes are not sufficiently fast, the associated surface processes may be significantly modified by the gravitational collapse. Our baseline scenario represents a stiffer orogen, whose post-collisional topographic evolution is not controlled by the strength of the crust (e.g., the Alps; Pusok & Kaus, 2015; Wolf et al., 2022). This is usually the case for orogens that are dominated by erosional processes and are strong enough to limit their growth, or whenever the plate dynamics are not sufficient strong to develop high amplitude topography (Pusok & Kaus, 2015).

In this study, we do not include surface processes. Processes such as erosion and sedimentation influence orogenic evolution and can interact nonlinearly with tectonic subsidence and uplift rates (Beaumont et al., 2001; Wolf et al., 2022). We chose not to include these effects because the main objective of our work is to isolate the tectonic forcing and extract the associated surface deformation rates, providing a reference range for more specialized

21699356, 2026, 5, Downloaded from https://agupubs.onlinelibrary.wiley.com/doi/10.1029/2025JB032004 by Karlsruher Institut Fur Technologie, Wiley Online Library on [12/11/2026]. See the Terms and Conditions (https://onlinelibrary.wiley.com/terms-and-conditions) on Wiley Online Library for rules of use; OA articles are governed by the applicable Creative Commons License

21699356, 2026, 5, Downloaded from https://agupubs.onlinelibrary.wiley.com/doi/10.1029/2025JB032004 by Karlsruher Institut Fur Technologie, Wiley Online Library on [12/11/2026]. See the Terms and Conditions (https://onlinelibrary.wiley.com/terms-and-conditions) on Wiley Online Library for rules of use; OA articles are governed by the applicable Creative Commons License

studies (e.g., L. Eskens et al., 2025). Further research is needed to couple surface processes, basin evolution, and geodynamics.

Our simplified initial setup assumes a fully locked plate configuration. As shown by Wu et al. (2025), the interaction between these forces can induce additional convergence between the upper and lower plates, potentially magnifying the total uplift of the orogen.

5. Conclusion

Our experimental results highlight the importance of mantle rheology in the tearing dynamics. We find that the activation volume (i.e., the depth dependency of the mantle viscosity) has a first-order control over the process by hampering the stress evolution within the slab. We identified two end-member scenarios that show different spatio-temporal evolution and surface signal fingerprints. We show that the rate of necking and tearing processes is well correlated with surface velocities.

As a function of mantle rheology, the style of tearing continuously changes, reducing the magnitude of uplift and altering the spatial pattern. We can observe hypothesized tearing surface signals only if the mantle does not offer significant resistance to the necking process. However, in these cases, the timescales of breaking-off and tearing are fast enough that the time resolution of stratigraphical or thermo-chronological data cannot correctly resolve the entire evolution of the system. In the case of the slowest scenarios, uplift signals are challenging to isolate and can be easily overprinted by signals imposed by pre-existing structures (i.e., amount of subducted continental lithosphere).

The experiments that best fit the estimated tearing velocities are the slowest ones. These similarities are problematic because these experiments predict that surface signals are negligible. This indicate that surface signals might give a minimal estimate of the tearing velocities. We show that, as a function of mantle rheology, uplift signals can predate the tearing s.s. itself, and that further research is required to understand the shift between surface signals and tearing processes.

Conflict of Interest

The authors declare no conflicts of interest relevant to this study.

Availability Statement

All the scripts used to compile the data are available at https://zenodo.org/records/15464796 (Piccolo, 2025). The numerical calculations were performed using LaMEM (Popov & Kaus, 2025), and the visualizations were produced using Matplotlib (Caswell et al., 2021) and ParaView (Ahrens et al., 2005). We additionally used the Scientific Color Map tools (Crameri, 2023).

Acknowledgments

A.P. received funding from the DFG Grant TH 2076/7-1 awarded to M.T. and Royal Society Grant URF/R/231019 awarded to Timothy Craig. A.S. and M.T. received funding from DFG Grant TH 2076/8-1 awarded to M.T. P.R.E received funding from DFG Grant EI1176/1-1. L.H.J. Eskens and N.A.T. acknowledge support from DFG Grant TO 1364/1-1. We acknowledge also Laurent Jolivet and an anonymous reviewer for the useful comments that improved the quality of the current work.

References

Agard, P. (2021). Subduction of oceanic lithosphere in the Alps: Selective and archetypal from (slow-spreading) oceans. *Earth-Science Reviews*, *214*, 103517. https://doi.org/10.1016/j.earscirev.2021.103517

Ahrens, J., Geveci, B., & Law, C. (2005). *ParaView: An end-user tool for large-data visualization*. Elsevier.

Andrews, E. R., & Billen, M. I. (2009). Rheologic controls on the dynamics of slab detachment. *Tectonophysics*, *464*(1), 60–69. https://doi.org/10.1016/j.tecto.2007.09.004

Andrić-Tomašević, N., Koptev, A., Maiti, G., Gerya, T., & Ehlers, T. A. (2023). Slab tearing in non-collisional settings: Insights from thermo-mechanical modelling of oblique subduction. *Earth and Planetary Science Letters*, *610*, 118097. https://doi.org/10.1016/j.epsl.2023.118097

Ascione, A., Ciarcia, S., Di Donato, V., Mazzoli, S., & Vitale, S. (2012). The Pliocene-Quaternary wedge-top basins of southern Italy: An expression of propagating lateral slab tear beneath the Apennines. *Basin Research*, *24*(4), 456–474. https://doi.org/10.1111/j.1365-2117.2011.00534.x

Beaumont, C., Jamieson, R. A., Nguyen, M., & Lee, B. (2001). Himalayan tectonics explained by extrusion of a low-viscosity crustal channel coupled to focused surface denudation. *Nature*, *414*(6865), 738–742. https://doi.org/10.1038/414738a

Bellas, A., Zhong, S., Bercovici, D., & Mulyukova, E. (2018). Dynamic weakening with grain-damage and implications for slab detachment. *Physics of the Earth and Planetary Interiors*, *285*, 76–90. https://doi.org/10.1016/j.pepi.2018.09.001

Bercovici, D., Mulyukova, E., & Long, M. D. (2019). A simple toy model for coupled retreat and detachment of subducting slabs. *Journal of Geodynamics*, *129*, 275–289. https://doi.org/10.1016/j.jog.2018.03.002

Bercovici, D., Schubert, G., & Ricard, Y. (2015). Abrupt tectonics and rapid slab detachment with grain damage. *Proceedings of the National Academy of Sciences of the United States of America*, *112*(5), 1287–1291. https://doi.org/10.1073/pnas.1415473112

Boonma, K., García-Castellanos, D., Jiménez-Munt, I., & Gerya, T. (2023). Thermomechanical modelling of lithospheric slab tearing and its topographic response. *Frontiers in Earth Science*, *11*, 1095229. https://doi.org/10.3389/feart.2023.1095229

Burkett, E. R., & Billen, M. I. (2010). Three-dimensionality of slab detachment due to ridge-trench collision: Laterally simultaneous boudinage versus tear propagation. *Geochemistry, Geophysics, Geosystems*, *11*(11), Q11012. https://doi.org/10.1029/2010gc003286

Capitanio, F. (2014). The dynamics of extrusion tectonics: Insights from numerical modeling. *Tectonics*, *33*(12), 2361–2381. https://doi.org/10.1002/2014tc003688

Capitanio, F., & Replumaz, A. (2013). Subduction and slab breakoff controls on Asian indentation tectonics and Himalayan western syntaxis formation. *Geochemistry, Geophysics, Geosystems*, *14*(9), 3515–3531. https://doi.org/10.1002/ggge.20171

Capitanio, F., Replumaz, A., & Riel, N. (2015). Reconciling subduction dynamics during T ethys closure with large-scale A sian tectonics: Insights from numerical modeling. *Geochemistry, Geophysics, Geosystems*, *16*(3), 962–982. https://doi.org/10.1002/2014gc005660

Carminati, E., Wortel, M., Spakman, W., & Sabadini, R. (1998). The role of slab detachment processes in the opening of the western–central Mediterranean basins: Some geological and geophysical evidence. *Earth and Planetary Science Letters*, *160*(3–4), 651–665. https://doi.org/10.1016/s0012-821x(98)00118-6

Caswell, T. A., Droettboom, M., Lee, A., de Andrade, E. S., Hoffman, T., Hunter, J., et al. (2021). matplotlib/matplotlib: REL: v3.5.1. (Software). *Zenodo*. https://doi.org/10.5281/zenodo.5773480

Chatelain, J.-L., Molnar, P., Prévot, R., & Isacks, B. (1992). Detachment of part of the downgoing slab and uplift of the New Hebrides (Vanuatu) islands. *Geophysical Research Letters*, *19*(14), 1507–1510. https://doi.org/10.1029/92gl01389

Cosentino, D., Schildgen, T. F., Cipollari, P., Faranda, C., Gliozzi, E., Hudáčková, N., et al. (2012). Late Miocene surface uplift of the southern margin of the Central Anatolian Plateau, Central Taurides, Turkey. *Bulletin*, *124*(1–2), 133–145. https://doi.org/10.1130/b30466.1

Crameri, F. (2023). Scientific colour maps. (Software). *Zenodo*. https://doi.org/10.5281/zenodo.8409685

Crameri, F., Schmeling, H., Golabek, G. J., Duretz, T., Orendt, R., Buiter, S. J. H., et al. (2012). A comparison of numerical surface topography calculations in geodynamic modelling: An evaluation of the "sticky air" method. *Geophysical Journal International*, *189*(1), 38–54. https://doi.org/10.1111/j.1365-246x.2012.05388.x

Drucker, D. C., & Prager, W. (1952). Soil mechanics and plastic analysis or limit design. *Quarterly of Applied Mathematics*, *10*(2), 157–165. https://doi.org/10.1090/qam/48291

Duretz, T., Gerya, T. V., & May, D. A. (2011). Numerical modelling of spontaneous slab breakoff and subsequent topographic response. *Tectonophysics*, *502*(1–2), 244–256. https://doi.org/10.1016/j.tecto.2010.05.024

Duretz, T., Gerya, T. V., & Spakman, W. (2014). Slab detachment in laterally varying subduction zones: 3-D numerical modeling. *Geophysical Research Letters*, *41*(6), 1951–1956. https://doi.org/10.1002/2014GL059472

Duretz, T., Schmalholz, S. M., & Gerya, T. V. (2012). Dynamics of slab detachment. *Geochemistry, Geophysics, Geosystems*, *13*(3), Q03020. https://doi.org/10.1029/2011GC004024

Eskens, L., Piccolo, A., Thielmann, M., Claussmann, B., Lejri, M., Ehlers, T., & Andrić-Tomašević, N. (2025). The tectonostratigraphic expression of slab breakoff in foreland basins: Insights from 2D forward stratigraphic modeling. *Tectonics*, *44*(7), e2024TC008664. https://doi.org/10.1029/2024tc008664

Eskens, L. H., Andrić-Tomašević, N., Süss, P. M., Müller, M., Herrmann, R., & Ehlers, T. A. (2024). Lithospheric-and crustal-scale controls on variations in foreland basin development in the northern alpine foreland basin. *Tectonophysics*, *878*, 230283. https://doi.org/10.1016/j.tecto.2024.230283

Faccenda, M., Gerya, T. V., & Chakraborty, S. (2008). Styles of post-subduction collisional orogeny: Influence of convergence velocity, crustal rheology and radiogenic heat production. *Lithos*, *103*(1–2), 257–287. https://doi.org/10.1016/j.lithos.2007.09.009

Fellin, M. G., San Jose, M., Faccenna, C., Willett, S. D., Cosentino, D., Lanari, R., et al. (2022). Transition from slab roll-back to slab break-off in the central Apennines, Italy: Constraints from the stratigraphic and thermochronologic record. *GSA Bulletin*, *134*(7–8), 1916–1930. https://doi.org/10.1130/b36123.1

Ferrari, L. (2004). Slab detachment control on mafic volcanic pulse and mantle heterogeneity in central Mexico. *Geology*, *32*(1), 77–80. https://doi.org/10.1130/g19887.1

Forte, A. M., Yanites, B. J., & Whipple, K. X. (2016). Complexities of landscape evolution during incision through layered stratigraphy with contrasts in rock strength. *Earth Surface Processes and Landforms*, *41*(12), 1736–1757. https://doi.org/10.1002/esp.3947

Fox, M., Herman, F., Willett, S. D., & Schmid, S. M. (2016). The exhumation history of the European Alps inferred from linear inversion of thermochronometric data. *American Journal of Science*, *316*(6), 505–541. https://doi.org/10.2475/06.2016.01

Garzanti, E., Radeff, G., & Malusà, M. G. (2018). Slab breakoff: A critical appraisal of a geological theory as applied in space and time. *Earth-Science Reviews*, *177*, 303–319. https://doi.org/10.1016/j.earscirev.2017.11.012

Gerya, T. V., Yuen, D. A., & Maresch, W. V. (2004). Thermomechanical modelling of slab detachment. *Earth and Planetary Science Letters*, *226*(1–2), 101–116. https://doi.org/10.1016/j.epsl.2004.07.022

Haq, B. U., Hardenbol, J., Vail, P. R., Stover, L., Colin, J., Ioannides, N., et al. (1988). Mesozoic and Cenozoic chronostratigraphy and cycles of sea-level change.

Hirth, G., & Kohlstedt, D. (2003). Rheology of the upper mantle and the mantle wedge: A view from the experimentalists. In *Geophysical monograph-American geophysical union* (Vol. 138, pp. 83–106).

Isacks, B., & Molnar, P. (1969). Mantle earthquake mechanisms and the sinking of the lithosphere. *Nature*, *223*(5211), 1121–1124. https://doi.org/10.1038/2231121a0

Isacks, B., Oliver, J., & Sykes, L. R. (1968). Seismology and the new global tectonics. *Journal of Geophysical Research*, *73*(18), 5855–5899.

Kaus, B. J. P., Popov, A. A., Baumann, T., Pusok, A., Bauville, A., Fernandez, N., & Collignon, M. (2016). Forward and inverse modelling of lithospheric deformation on geological timescales. In *Proceedings of NIC symposium* (Vol. 48, pp. 978–983). John von Neumann Institute for Computing (NIC), NIC Series.

Koulakov, I., Zaharia, B., Enescu, B., Radulian, M., Popa, M., Parolai, S., & Zschau, J. (2010). Delamination or slab detachment beneath Vrancea? New arguments from local earthquake tomography. *Geochemistry, Geophysics, Geosystems*, *11*(3), Q03002. https://doi.org/10.1029/2009GC002811

Kufner, S.-K., Kakar, N., Bezada, M., Bloch, W., Metzger, S., Yuan, X., et al. (2021). The Hindu Kush slab break-off as revealed by deep structure and crustal deformation. *Nature Communications*, *12*(1), 1685. https://doi.org/10.1038/s41467-021-21760-w

Kufner, S. K., Schurr, B., Haberland, C., Zhang, Y., Saul, J., Ischuk, A., & Oimahmadov, I. (2017). Zooming into the Hindu Kush slab break-off: A rare glimpse on the terminal stage of subduction. *Earth and Planetary Science Letters*, *461*, 127–140. https://doi.org/10.1016/j.epsl.2016.12.043

Kuhlemann, J. (2007). Paleogeographic and paleotopographic evolution of the Swiss and Eastern Alps since the Oligocene. *Global and Planetary Change*, *58*(1–4), 224–236. https://doi.org/10.1016/j.gloplacha.2007.03.007

Leeder, M. R., Harris, T., & Kirkby, M. J. (1998). Sediment supply and climate change: Implications for basin stratigraphy. *Basin Research*, *10*(1), 7–18. https://doi.org/10.1046/j.1365-2117.1998.00054.x

21699356, 2026, 5, Downloaded from https://agupubs.onlinelibrary.wiley.com/doi/10.1029/2025JB032004 by Karlsruher Institut Fur Technologie, Wiley Online Library on [12/11/2026]. See the Terms and Conditions (https://onlinelibrary.wiley.com/terms-and-conditions) on Wiley Online Library for rules of use; OA articles are governed by the applicable Creative Commons License

Magni, V., Faccenna, C., van Hunen, J., & Funiciello, F. (2013). Delamination vs. break-off: The fate of continental collision. *Geophysical Research Letters*, *40*(2), 285–289. https://doi.org/10.1002/grl.50090

Maiti, G., Koptev, A., Baville, P., Gerya, T., Crosetto, S., & Andrić-Tomašević, N. (2024). Topography response to horizontal slab tearing and oblique continental collision: Insights from 3D thermomechanical modeling. *Journal of Geophysical Research: Solid Earth*, *129*(10), e2024JB029385. https://doi.org/10.1029/2024JB029385

McKenzie, D. P. (1969). Speculations on the consequences and causes of plate motions. *Geophysical Journal of the Royal Astronomical Society*, *18*(1), 1–32. https://doi.org/10.1111/j.1365-246X.1969.tb00259.x

Menant, A., Sternai, P., Jolivet, L., Guillou-Frottier, L., & Gerya, T. (2016). 3D numerical modeling of mantle flow, crustal dynamics and magma genesis associated with slab roll-back and tearing: The eastern Mediterranean case. *Earth and Planetary Science Letters*, *442*, 93–107. https://doi.org/10.1016/j.epsl.2016.03.002

Meulenkamp, J., Kováč, M., & Cicha, I. (1996). On late Oligocene to Pliocene depocentre migrations and the evolution of the Carpathian-Pannonian system. *Tectonophysics*, *266*(1–4), 301–317. https://doi.org/10.1016/s0040-1951(96)00195-3

Mitrofan, H., Anghelache, M. A., Chitea, F., Damian, A., Cadicheanu, N., & Vişan, M. (2016). Lateral detachment in progress within the Vrancea slab (Romania): Inferences from intermediate-depth seismicity patterns. *Geophysical Journal International*, *205*(2), 864–875. https://doi.org/10.1093/gji/ggv533

Piccolo, A. (2025). Data and scripts for "the dynamics and surface signal of slab break-off in continental settings: Insights from 3D numerical modelling". [Dataset]. *Zenodo*. https://doi.org/10.5281/zenodo.15464796

Piccolo, A., Faccenda, M., Carosi, R., Montomoli, C., & Visonà, D. (2018). Crustal strength control on structures and metamorphism in collisional orogens. *Tectonophysics*, *746*, 470–492. https://doi.org/10.1016/j.tecto.2017.09.018

Popov, A., & Kaus, B. (2025). Lamem. (Software). *Zenodo*. https://doi.org/10.5281/zenodo.15524303

Pusok, A., & Kaus, B. J. (2015). Development of topography in 3-D continental-collision models. *Geochemistry, Geophysics, Geosystems*, *16*(5), 1378–1400. https://doi.org/10.1002/2015gc005732

Ribe, N. M. (2010). Bending mechanics and mode selection in free subduction: A thin-sheet analysis. *Geophysical Journal International*, *180*(2), 559–576. https://doi.org/10.1111/j.1365-246X.2009.04460.x

Ribe, N. M., & Xu, B. (2020). Subduction of non-Newtonian plates: Thin-sheet dynamics of slab necking and break-off. *Geophysical Journal International*, *220*(2), 910–927. https://doi.org/10.1093/gji/ggz500

Rybacki, E., & Dresen, G. (2000). Dislocation and diffusion creep of synthetic anorthite aggregates. *Journal of Geophysical Research*, *105*(B11), 26017–26036. https://doi.org/10.1029/2000jb900223

Schildgen, T. F., Yıldırım, C., Cosentino, D., & Strecker, M. R. (2014). Linking slab break-off, Hellenic trench retreat, and uplift of the Central and Eastern Anatolian plateaus. *Earth-Science Reviews*, *128*, 147–168. https://doi.org/10.1016/j.earscirev.2013.11.006

Schlunegger, F., & Kissling, E. (2015). Slab rollback orogeny in the Alps and evolution of the Swiss Molasse basin. *Nature Communications*, *6*(1), 8605. https://doi.org/10.1038/ncomms9605

Schmalholz, S. M. (2011). A simple analytical solution for slab detachment. *Earth and Planetary Science Letters*, *304*(1–2), 45–54. https://doi.org/10.1016/j.epsl.2011.01.011

Spakman, W., & Wortel, R. (2004). A tomographic view on western Mediterranean geodynamics. In W. Cavazza, F. Roure, W. Spakman, G. M. Stampfli, & P. A. Ziegler (Eds.), *The TRANSMED atlas. The Mediterranean region from crust to mantle: Geological and geophysical framework of the Mediterranean and the surrounding areas* (pp. 31–52). Springer Berlin Heidelberg. https://doi.org/10.1007/978-3-642-18919-7_2

Spang, A., Baumann, T. S., & Kaus, B. J. (2021). A multiphysics approach to constrain the dynamics of the Altiplano-Puna magmatic system. *Journal of Geophysical Research: Solid Earth*, *126*(7), e2021JB021725. https://doi.org/10.1029/2021jb021725

Spang, A., Thielmann, M., & Kiss, D. (2024). Rapid ductile strain localization due to thermal runaway. *Journal of Geophysical Research: Solid Earth*, *129*(10), e2024JB028846. https://doi.org/10.1029/2024JB028846

Sperner, B., Lorenz, F., Bonjer, K., Hettel, S., Müller, B., & Wenzel, F. (2001). Slab break-off—Abrupt cut or gradual detachment? New insights from the Vrancea Region (SE Carpathians, Romania). *Terra Nova*, *13*(3), 172–179. https://doi.org/10.1046/j.1365-3121.2001.00335.x

Sternai, P., Jolivet, L., Menant, A., & Gerya, T. (2014). Driving the upper plate surface deformation by slab rollback and mantle flow. *Earth and Planetary Science Letters*, *405*, 110–118. https://doi.org/10.1016/j.epsl.2014.08.023

Sternai, P., Sue, C., Husson, L., Serpelloni, E., Becker, T. W., Willett, S. D., et al. (2019). Present-day uplift of the European Alps: Evaluating mechanisms and models of their relative contributions. *Earth-Science Reviews*, *190*, 589–604. https://doi.org/10.1016/j.earscirev.2019.01.005

Sun, M., & Bezada, M. (2020). Seismogenic necking during slab detachment: Evidence from relocation of intermediate-depth seismicity in the Alboran slab. *Journal of Geophysical Research: Solid Earth*, *125*(2), e2019JB017896. https://doi.org/10.1029/2019JB017896

Thielmann, M. (2018). Grain size assisted thermal runaway as a nucleation mechanism for continental mantle earthquakes: Impact of complex rheologies. *Tectonophysics*, *746*, 611–623. https://doi.org/10.1016/j.tecto.2017.08.038

Thielmann, M., & Schmalholz, S. M. (2020). Contributions of grain damage, thermal weakening, and necking to slab detachment. *Frontiers in Earth Science*, *8*, 254. https://doi.org/10.3389/feart.2020.00254

Ton, S. Y. A., & Wortel, M. J. (1997). Slab detachment in continental collision zones: An analysis of controlling parameters. *Geophysical Research Letters*, *24*(16), 2095–2098. https://doi.org/10.1029/97gl01939

Turcotte, D., & Schubert, G. (2014). *Geodynamics*. Cambridge University Press.

van Hunen, J., & Allen, M. B. (2011). Continental collision and slab break-off: A comparison of 3-D numerical models with observations. *Earth and Planetary Science Letters*, *302*(1–2), 27–37. https://doi.org/10.1016/j.epsl.2010.11.035

Von Blanckenburg, F., & Davies, J. H. (1995). Slab breakoff: A model for syncollisional magmatism and tectonics in the Alps (Technical Report No. 1). *Tectonics*, *14*(1), 120–131. https://doi.org/10.1029/94tc02051

Von Tscharner, M., Schmalholz, S., & Duretz, T. (2014). Three-dimensional necking during viscous slab detachment. *Geophysical Research Letters*, *41*(12), 4194–4200. https://doi.org/10.1002/2014gl060075

Wolf, S. G., Huismans, R. S., Braun, J., & Yuan, X. (2022). Topography of mountain belts controlled by rheology and surface processes. *Nature*, *606*(7914), 516–521. https://doi.org/10.1038/s41586-022-04700-6

Wortel, M., & Spakman, W. (2000). Subduction and slab detachment in the Mediterranean-Carpathian region. *Science*, *290*(5498), 1910–1917. https://doi.org/10.1126/science.290.5498.1910

Wu, Y., Faccenda, M., Liao, J., Fan, J., Guo, F., & Lai, Z. (2025). Mantle-driven plate convergence due to slab detachment. *Communications Earth & Environment*, *6*(1), 494. https://doi.org/10.1038/s43247-025-02484-x

Yoshioka, S., & Wortel, M. J. R. (1995). Three-dimensional numerical modeling of detachment of subducted lithosphere. *Journal of Geophysical Research*, *100*(B10), 20223–20244. https://doi.org/10.1029/94JB01258doi:10.1029/94JB01258

21699356, 2026, 5, Downloaded from https://agupubs.onlinelibrary.wiley.com/doi/10.1029/2025JB032004 by Karlsruher Institut Fur Technologie, Wiley Online Library on [12/11/2026]. See the Terms and Conditions (https://onlinelibrary.wiley.com/terms-and-conditions) on Wiley Online Library for rules of use; OA articles are governed by the applicable Creative Commons License